

Transition-Path Theory and Path-Finding Algorithms for the Study of Rare Events

Weinan E¹ and Eric Vanden-Eijnden²

¹Department of Mathematics and Program in Applied and Computational Mathematics,
Princeton University, Princeton, New Jersey 08544; email: weinan@princeton.edu

²Courant Institute of Mathematical Sciences, New York University, New York, New York 10012;
email: eve2@courant.nyu.edu

Annu. Rev. Phys. Chem. 2010. 61:391–420

First published online as a Review in Advance on
January 4, 2010

The *Annual Review of Physical Chemistry* is online at
physchem.annualreviews.org

This article's doi:
10.1146/annurev.physchem.040808.090412

Copyright © 2010 by Annual Reviews.
All rights reserved

0066-426X/10/0505-0391\$20.00

Key Words

string method, activated process, minimum free energy path,
transition-state theory

Abstract

Transition-path theory is a theoretical framework for describing rare events in complex systems. It can also be used as a starting point for developing efficient numerical algorithms for analyzing such rare events. Here we review the basic components of transition-path theory and path-finding algorithms. We also discuss connections with the classical transition-state theory.

1. INTRODUCTION

The study of rare events is one of the most fundamental problems in chemistry. Chemical reactions, conformation changes of molecules, and quantum tunneling are all examples of rare events. These events are rare because the system has to overcome some barriers, which can either be of an energetic or an entropic nature.

From a theoretical viewpoint, the well-known transition-state theory (TST) (1–3), a cornerstone of chemical physics, has been successful in providing the language, the intuition, and the foundation for the development of computational tools for studying barrier-crossing events. What is most attractive about TST is its simplicity: It states basically that to move from the reactant state to the product state, the system has to navigate itself to the transition state, which is a saddle point on the potential energy surface. In addition, one can obtain the transition rate by computing the probability flux of particles that cross the dividing surface, which contains the transition state and separates the basins of attraction of the reactant and product states. In many cases, one can also define the most probable transition path for the reaction, which for overdamped systems is simply the minimum energy path (MEP).

It has also been realized for some time that TST is limited to situations in which the potential energy surface is rather smooth and the crossing through the transition-state region is ballistic, as it assumes that every crossing gives rise to a successful reaction. If the crossing is diffusive, then TST overestimates the reaction rate. To correct the TST rate, investigators have introduced the concept of a transmission coefficient, which gives the probability of successful reactions among all crossings (4–7). This coefficient fixes the difficulties with the inaccuracy of the TST rates, but it also increases the complexity of the computational algorithm substantially. In addition, it gives little information on the nature of the rare event besides its rate.

The situation is actually a bit worse. For a system with a rugged potential energy landscape, or when entropic (i.e., volume) effects matter (as they typically do in high dimensions), the saddle points do not necessarily play the role of transition states. One idea, known as the variational TST, is to optimize over the dividing surfaces or dividing hyperplanes to identify the one with the maximum transmission coefficient. However, it is not clear how effective this approach is. In fact, in complex situations, the very notion of the transition state becomes obscure.

Another popular line of thought is to consider the free energy surface instead of the potential energy surface, because the free energy surface is typically much more smooth. However, to define the free energy, one must have a set of collective variables to begin with, and therefore the concept of reaction coordinates has been introduced. Intuitively, reaction coordinates should be something that can be used to parameterize the reaction paths. This is certainly a useful notion, but it is also one that has been greatly abused: Often one has to guess what the reaction coordinates are based on intuition, and there are plenty of examples showing that our intuition does not always serve us in the right way. In particular, the slow variables may not have anything to do with the reaction coordinates (8).

A different viewpoint was pioneered by Pratt (9) and developed much further (10, 11) in a transition-path sampling (TPS) technique. Instead of focusing on the transition states, TPS focuses on the ensemble of transition paths, i.e., those pieces of trajectories by which the rare event occurs, and thereby tries to identify transition mechanisms and compute transition rates. Indeed, TPS is a way of Monte Carlo sampling the transition-path ensemble.

TPS is a nice numerical technique, but it still leaves open the question of what should replace TST for systems with rugged energy landscapes or when the barriers are of entropic origin. Being pieces of actual trajectories, the transition paths can be quite complicated and uninformative per se, especially in high-dimensional systems. This calls for a statistical mechanics framework to analyze the transition-path ensemble.

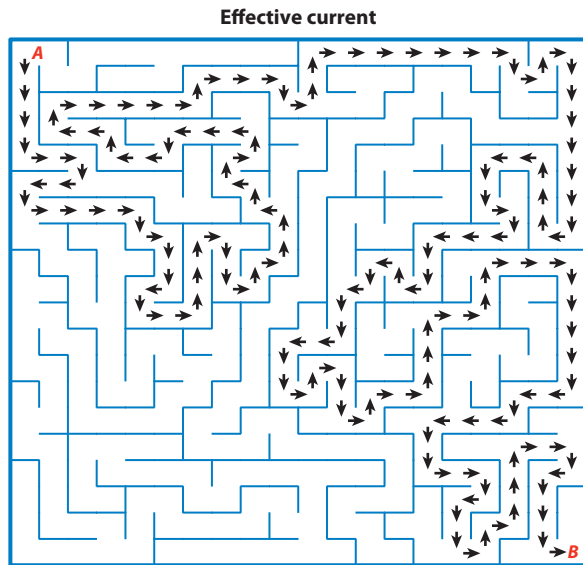


Figure 1

The maze example. Although there is a well-defined shortest path from the entrance *A* to the exit *B* (indicated by the arrows), a random walker in the maze is oblivious to this path. The transition state is located midway along the shortest path, i.e., somewhere near the upper-right corner, but it is uninformative per se. Even the reactive paths, i.e., those paths that go from *A* to *B* without going back to *A* in between (which are the objects sampled by transition-path sampling), mostly aimlessly wander the maze. Transition-path theory is designed to handle situations like this one. It not only calculates the rate of the reaction, but also characterizes its mechanism without having to sample reactive trajectories beforehand, e.g., by calculating the probability current of the reactive paths (shown by the arrows). In this case, the current concentrates on the shortest path and is zero elsewhere.

Some difficulties are already captured by the maze example shown in **Figure 1**. Imagine a random walker trying to reach the product state *B* on one end starting from the reactant state *A* on the other. Although there is indeed a shortest path connecting these two states, the walker is oblivious to it. In most cases, starting from *A*, the walker will get lost in the many dead ends of the maze before returning often to *A* without reaching *B*. Even if we focus on the paths that do reach *B* before going back to *A*—i.e., the reactive paths sampled by TPS—these paths also wander in the maze in a complex fashion, and extracting useful information from them, such as the shortest path or the reaction rate, is nontrivial. In this example, the transition state is located midway along the shortest path, but this state alone is rather uninformative—knowing that one is midway in a maze does not provide much information about where to go next. How can we efficiently compute the transition rate in such an example? How can we understand the mechanism of the reaction and get the shortest path, for example, without having to sample reactive paths beforehand?

Addressing these questions, not only in the maze example but in full generality, was the main motivation for the development of transition-path theory (TPT) in Reference 12 (see also 13–15) and is also the primary focus of this review. Roughly speaking, TPT is a theoretical tool for analyzing the transition-path ensemble. Intuitively, for systems with rugged energy landscapes, one would like to replace the notion of a transition state by the notion of a transition-state ensemble and to replace the notion of most probable transition paths by that of transition tubes (inside which most of the flux of the transition paths is concentrated—this is the shortest path in the maze example, and is one of the objects that TPT calculates). TPT allows the formulation of such

intuitive notions precisely. It addresses questions such as the following: (a) What is the probability distribution of the particles in the transition-path ensemble? (b) What is the transition rate? (c) What is the probability current associated with the transition paths? TPT is exact regardless of the complexity of the reaction, and it provides a much more complete picture of the reaction than TST does. In principle, it permits one to bypass altogether the sampling of the reactive paths done in TPS.

Being exact, TPT provides the foundation for making approximations and developing efficient numerical algorithms. For example, the string method (16–22), which is a rather powerful tool for analyzing transitions in systems with rough energy landscapes, can be derived from TPT under the approximation that with high probability, the flux associated with the transition paths is concentrated inside one or a few thin tubes. One can envision other approximations, which will lead to other numerical algorithms. Both the theoretical aspects of TPT and the path-finding algorithms to which it leads are reviewed below. An extended version of this review is also available (8).

2. TRANSITION-PATH THEORY

2.1. The Setup

We first introduce the kind of dynamics that we consider. For the most part, we focus on systems governed by the Langevin equation

$$\begin{cases} \dot{\mathbf{x}} = m^{-1}\mathbf{p}, \\ \dot{\mathbf{p}} = -\nabla U - \gamma\mathbf{p} + \sqrt{2\gamma k_B T} m^{1/2} \dot{\mathbf{w}}, \end{cases} \quad (1)$$

where m is the mass matrix, and U denotes the potential energy of the system. The last two terms in the second equation are thermostat terms that represent the effects of the heat bath: γ is the friction coefficient, which can also be a tensor although we only consider the case when it is a scalar; T is the temperature; k_B is the Boltzmann constant; and $\dot{\mathbf{w}}$ is the standard Gaussian white noise, i.e., the Gaussian process with mean 0 and covariance

$$\langle \dot{w}_i(t) \dot{w}_j(s) \rangle = \delta_{ij} \delta(t-s). \quad (2)$$

One may also consider other thermostats (such as the ones proposed in References 23 and 24), as well as other ensembles (e.g., NPT) (25). Formally, one may also consider the special case where $\gamma = 0$, corresponding to the NVE ensemble, in which Equation 1 reduces to the Hamiltonian dynamics, with no explicit noise:

$$\begin{cases} \dot{\mathbf{x}} = m^{-1}\mathbf{p}, \\ \dot{\mathbf{p}} = -\nabla U. \end{cases} \quad (3)$$

In this case, the chaotic nature of the dynamics plays the role of the noise, and indeed one typically uses the Langevin equation (Equation 1) with a friction coefficient small enough that the solutions of Equation 1 do not look different from the ones of Equation 3. Another limit of Equation 1, which is probably less relevant in applications but is useful for discussing concepts, is the overdamped dynamics obtained when $\gamma \gg 1$:

$$\gamma m \dot{\mathbf{x}} = -\nabla U + \sqrt{2\gamma k_B T} m^{1/2} \dot{\mathbf{w}}. \quad (4)$$

More generally, we consider the stochastic process $\mathbf{z} \in \Omega \subset \mathbb{R}^d$ described by the Itô stochastic differential equation:

$$\dot{\mathbf{z}} = \mathbf{b}(\mathbf{z}) + \sqrt{2} \sigma(\mathbf{z}) \dot{\mathbf{w}}. \quad (5)$$

We also assume that the dynamics defined by Equation 5 is ergodic and has a unique invariant distribution, i.e., a probability distribution that is preserved by the dynamics. We denote the density of this distribution by ρ . When the dynamics obeys detailed balance, this invariant distribution is simply the equilibrium distribution. For example, when the dynamics is governed by Equation 4, the density of the invariant or equilibrium distribution is simply

$$\rho(\mathbf{x}) = Z^{-1} e^{-\beta U(\mathbf{x})}, \quad (6)$$

where $Z = \int e^{-\beta U(\mathbf{x})} d\mathbf{x}$.

2.2. The Main Objects in Transition-Path Theory

Given two sets A and B in phase space (viewed as reactant and product states, respectively), TPT analyzes the reaction from A to B by characterizing the statistical properties of the transition paths by which this reaction occurs. More precisely, if we consider an infinitely long trajectory $\mathbf{z}(t)$ with $t \geq 0$, we can cut from this trajectory the pieces in which the trajectory is moving from A to B without returning to A in between (see **Figure 2** for a schematic illustration). We refer to these pieces as a reactive trajectory from A to B , an A - B reactive trajectory, or a transition path from A to B , and we refer to the set of transition paths as the transition-path ensemble from A to B . This ensemble is closely related to the one considered in TPS, except that there is no restriction on the length of the reactive trajectories. Given the trajectory $\mathbf{z}(t)$ with $t \geq 0$, we denote by R the set of times at which $\mathbf{z}(t)$ belongs to an A - B reactive path. The following subsections address several questions for the transition-path ensemble.

2.2.1. Where do these paths spend their time? We are looking for a density $\rho_R(\mathbf{z})$ that gives the probability density of finding a reactive trajectory at \mathbf{z} . In the setup described above, $\rho_R(\mathbf{z})$ can be defined via

$$\rho_R(\mathbf{z}) = \lim_{T \rightarrow \infty} \frac{1}{T} \int_0^T \delta(\mathbf{z} - \mathbf{z}(t)) \mathbf{1}_R(t) dt, \quad (7)$$

where $\mathbf{1}_R(t) = 1$ if $t \in R$ [i.e., at time t , $\mathbf{z}(t)$ belongs to an A - B reactive path] and $\mathbf{1}_R(t) = 0$ otherwise. If we consider the whole trajectory (not just the reactive pieces) and ask the same question, then the probability density obtained is the density $\rho(\mathbf{z})$ of the invariant distribution:

$$\rho(\mathbf{z}) = \lim_{T \rightarrow \infty} \frac{1}{T} \int_0^T \delta(\mathbf{z} - \mathbf{z}(t)) dt. \quad (8)$$

We also note that $\rho_R(\mathbf{z})$ is not normalized: The total integral of $\rho_R(\mathbf{z})$ gives the probability of being A - B reactive.

The density $\rho_R(\mathbf{z})$ gives information about the likelihood of the A - B reactive paths going through a given region, but not about how they move from region to region. To characterize how

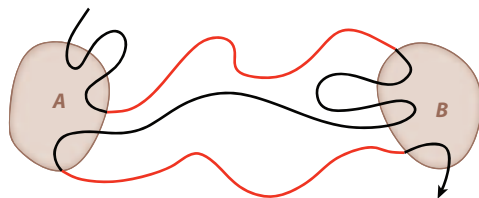


Figure 2

Schematic illustration of a long trajectory oscillating between the reactant state A and the product state B . The reactive pieces of this trajectory, during which the system travels from A to B , are shown in red.

these paths flow from A to B on average, we need another quantity, namely their probability current. To understand how the probability current comes about, let us consider first the instantaneous probability density $\rho(\mathbf{z}, t)$ of the (full) process $\mathbf{z}(t)$. Formally, this probability density can be defined as

$$\rho(\mathbf{z}, t) = \langle \delta(\mathbf{z} - \mathbf{z}(t)) \rangle, \quad (9)$$

where the brackets denote the expectation with respect to the realizations of the noise in Equation 5. Differentiating Equation 9 with respect to time, we can write¹

$$\frac{\partial}{\partial t} \rho(\mathbf{z}, t) = -\langle \dot{\mathbf{z}}(t) \cdot \nabla \delta(\mathbf{z} - \mathbf{z}(t)) \rangle \equiv -\nabla \cdot \mathbf{J}(\mathbf{z}, t), \quad (10)$$

which defines the instantaneous probability current

$$\mathbf{J}(\mathbf{z}, t) = \langle \dot{\mathbf{z}}(t) \delta(\mathbf{z} - \mathbf{z}(t)) \rangle. \quad (11)$$

Equation 10 has the form of a conservation law (the total probability being the quantity that is conserved). The ergodicity assumption implies that $\rho(\mathbf{z}, t) \rightarrow \rho(\mathbf{z})$ as $t \rightarrow \infty$. In turn, this implies that $\mathbf{J}(\mathbf{z}, t) \rightarrow \mathbf{J}(\mathbf{z})$, which is the steady-state current defined by

$$\mathbf{J}(\mathbf{z}) = \lim_{T \rightarrow \infty} \frac{1}{T} \int_0^T \dot{\mathbf{z}}(t) \delta(\mathbf{z} - \mathbf{z}(t)) dt. \quad (12)$$

It is easy to see that

$$J_i(\mathbf{z}) = b_i(\mathbf{z})\rho(\mathbf{z}) - \sum_{j=1}^d \frac{\partial}{\partial z_j} (a_{i,j}(\mathbf{z})\rho(\mathbf{z})). \quad (13)$$

For equilibrium systems, $\mathbf{J}(\mathbf{z}) = 0$. For nonequilibrium steady states, however, $\mathbf{J}(\mathbf{z})$ may not vanish. This suggests that we need to ask the same question for the A - B reactive paths.

2.2.2. What is the current associated with the reactive trajectories? The current associated with the reactive paths is the vector field $\mathbf{J}_R : \Omega \mapsto \mathbb{R}^d$ defined as

$$\mathbf{J}_R(\mathbf{z}) = \lim_{T \rightarrow \infty} \frac{1}{T} \int_0^T \dot{\mathbf{z}}(t) \delta(\mathbf{z} - \mathbf{z}(t)) \mathbf{1}_R(t) dt. \quad (14)$$

This current must be divergence-free outside of A and B , but it does not vanish. Indeed, by construction, A is a source and B is a sink of reactive trajectories (there are no other sources or sinks of reactive trajectories). The flow lines of $\mathbf{J}_R(\mathbf{z})$ indicate how the reactive trajectories go from A to B on average. The current $\mathbf{J}_R(\mathbf{z})$ is also useful for answering the question posed in Section 2.2.3.

2.2.3. What is the reaction rate? If N_T is the number of A - B reactive trajectories [of the given trajectory $\mathbf{z}(t)$] in $[0, T]$, what is the limit of N_T/T as $T \rightarrow \infty$? This is the reaction rate

$$\nu_R = \lim_{T \rightarrow \infty} \frac{N_T}{T}, \quad (15)$$

which is the total probability flux of reactive trajectories out of A and into B and [as $\mathbf{J}_R(\mathbf{z})$ is divergence-free] is also the probability flux through any dividing surface S leaving A on one side

¹These manipulation require interpreting the various products in the Stratonovich sense so that standard differentiation rules apply. This is just a technical point, however.

and B on the other:

$$\nu_R = \int_S \hat{\mathbf{n}}_S(\mathbf{z}) \cdot \mathbf{J}_R(\mathbf{z}) d\sigma_S(\mathbf{z}). \quad (16)$$

Here $\hat{\mathbf{n}}_S(\mathbf{z})$ is the unit normal to S pointing toward B , and $d\sigma_S(\mathbf{z})$ is the surface element in S . Another expression for ν_R is given below (see Equation 31). ν_R is also the rate of the backreaction from B to A . Indeed, each time the process makes a transition from A to B , it needs to make a transition from B to A before making another transition from A to B ; i.e., the number of A - B trajectories in $[0, T]$ is the same as the number of B - A trajectories plus or minus one. Of course, this does not mean that the average time it takes the process to go to B starting from A is the same as the time it takes to go to A starting from B . To compute these average times, we let T_A be the total time in $[0, T]$ during which the last set hit by the trajectory was A , and T_B be the total time during which the last set was B . Then $T_A + T_B = T$, and we can define the rates as

$$k_{A,B} = \lim_{T \rightarrow \infty} \frac{N_T}{T_A}, \quad k_{B,A} = \lim_{T \rightarrow \infty} \frac{N_T}{T_B}. \quad (17)$$

These two rates differ (and are different from ν_R), and their inverses give an estimate of the average transition times from A to B and B to A . Below we explain how to compute the rates given in Equation 17 and relate them to ν_R .

2.3. The Committor Functions

To answer the questions listed in Section 2.2, we need the notion of committor functions, which are also referred to as capacitance functions in the mathematics literature (26, 27).

We let $q_+ : \Omega \mapsto [0, 1]$ be the solution of

$$\begin{cases} Lq_+ := \mathbf{b} \cdot \nabla q_+ + a : \nabla \nabla q_+ = 0, & \mathbf{z} \notin A \cup B, \\ q_+ = 0, & \mathbf{z} \in A, \\ q_+ = 1, & \mathbf{z} \in B. \end{cases} \quad (18)$$

The function q_+ is called the forward committor function for the transition process from A to B . In a similar fashion, we can define the backward committor function $q_- : \Omega \mapsto [0, 1]$ as the solution of

$$\begin{cases} L^\dagger q_- := -\mathbf{b} \cdot \nabla q_- + \frac{2}{\rho} \operatorname{div}(a\rho) \cdot \nabla q_- + a : \nabla \nabla q_- = 0, & \mathbf{z} \notin A \cup B, \\ q_- = 1, & \mathbf{z} \in A, \\ q_- = 0, & \mathbf{z} \in B. \end{cases} \quad (19)$$

The committor functions have a simple interpretation (28): $q_+(\mathbf{z})$ is the probability that a trajectory initiated at \mathbf{z} will reach B before it reaches A , and $q_-(\mathbf{z})$ is the probability that a trajectory arriving at \mathbf{z} came from A (i.e., before arriving at \mathbf{z} , it left from A after it left from B). The isosurfaces of these functions are called isocommittor surfaces. The isosurface $\{\mathbf{z} : q_+(\mathbf{z}) = \frac{1}{2}\}$ is of particular interest: Points on this surface have an equal probability of first reaching A or B .

For equilibrium processes, however, $q_- = 1 - q_+$ because $L^\dagger = L$. This is the case, in particular, of the overdamped equation (Equation 4). The symmetry under time reversal implies that the committor function can be obtained from a minimization principle. In the case of the overdamped equation, this involves minimizing the objective function

$$I(q) = k_B T \gamma^{-1} Z^{-1} \int \sum_{i=1}^d m_i^{-1} \left(\frac{\partial q(\mathbf{x})}{\partial x_i} \right)^2 e^{-\beta U(\mathbf{x})} d\mathbf{x} \quad (20)$$

over all q such that $q(\mathbf{x}) = 0$ if $\mathbf{x} \in A$ and $q(\mathbf{x}) = 1$ if $\mathbf{x} \in B$. For nonequilibrium processes, $q_- \neq 1 - q_+$ because $L^\dagger \neq L$ (the process is not statistically invariant under time reversal). In particular, for the Langevin equation (Equation 1), $q_-(\mathbf{x}, \mathbf{p}) \neq 1 - q_+(\mathbf{x}, \mathbf{p})$ because time reversal involves a momentum flip. In fact, $q_-(\mathbf{x}, \mathbf{p}) = 1 - q_+(\mathbf{x}, -\mathbf{p})$.

The committor functions (Equations 18 and 19) cannot be solved in closed form except in the simplest cases. One such case is that of the overdamped equation in one dimension, in which Equation 18 reduces to

$$k_B T q_+'' - U' q_+' = 0, \quad (21)$$

where the prime denotes the derivative with respect to x . The solution of Equation 21 with the boundary condition $q_+(a) = 0$, $q_+(b) = 1$ with $a \leq b$ (i.e., $A = \{x \leq a\}$ and $B = \{x \geq b\}$) is

$$q(x) = \frac{\int_a^x e^{\beta U(x')} dx'}{\int_a^b e^{\beta U(x')} dx'}. \quad (22)$$

In particular, if $U(x)$ is a double-well potential with a barrier much higher than $k_B T = 1/\beta$, and a and b are two points at the bottom of the wells [e.g., $U(x) = (1 - x^2)^2$, $a = -1$ and $b = 1$], then the function $q(x)$ is close to zero on the left side of the barrier and close to 1 on the right side, and it goes rapidly from 0 to 1 in the region near the top of the barrier. In particular, $q(x) = \frac{1}{2}$ is attained close to the barrier top.

For more complicated situations, the committor functions have to be found numerically. Below, we use the rugged Mueller potential in two dimensions (shown in **Figure 3**) for illustration. The isocommittor curves are shown in **Figure 4** for this example in the case of overdamped dynamics. Other low-dimensional examples, such as those involving multiple pathways, entropic effects, and Langevin dynamics, are discussed in Reference 13.

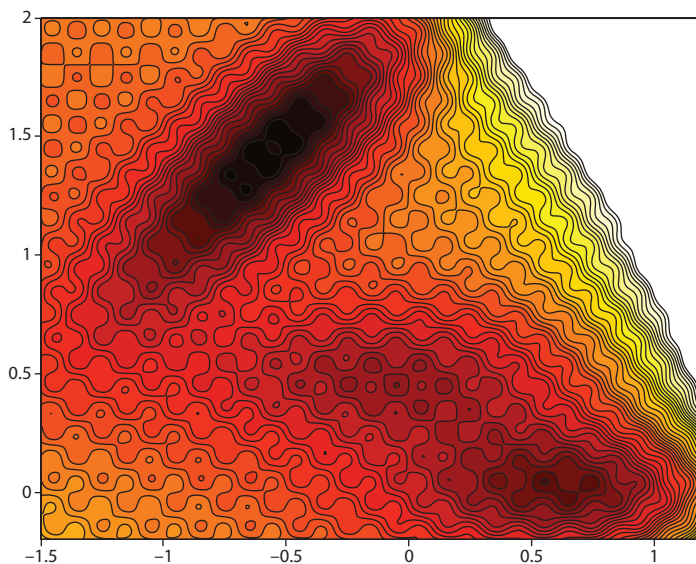


Figure 3

Contour lines of the rugged Mueller potential. The darker the region is, the lower the potential.

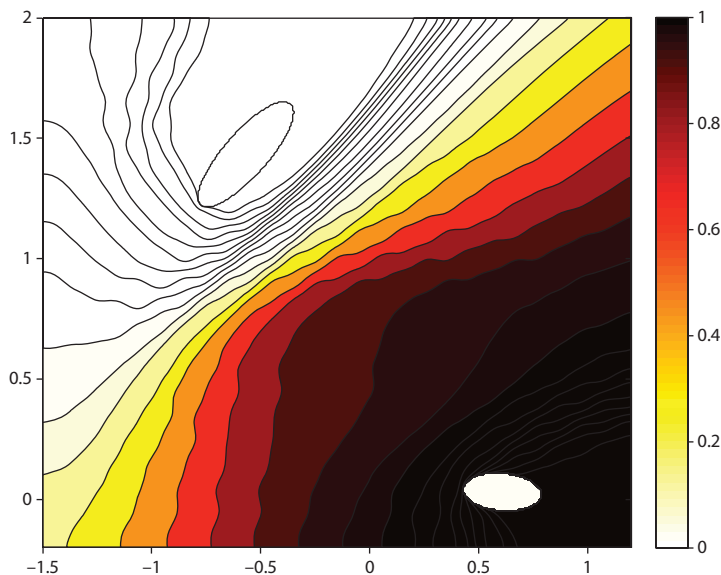


Figure 4

Contour lines of a committor function in the rugged Mueller potential. The reactant state A is the ellipse in the upper-left corner; the product state is the ellipse in the lower-right corner. Both sets are regions where the potential shown in **Figure 3** is relatively low.

2.4. Probability Density of Reactive Trajectories

Using the Markov nature of the dynamics, one can easily see that the probability density of finding a reactive trajectory at \mathbf{z} can be expressed as the product between $\rho(\mathbf{z})$ (which gives the probability density of finding a trajectory at \mathbf{z}) and $q_+(\mathbf{z})q_-(\mathbf{z})$ (which gives the probability that the trajectory came last from A and will go next to B ; i.e., that it is A - B reactive). As a result,

$$\rho_R(\mathbf{z}) = q_+(\mathbf{z})q_-(\mathbf{z})\rho(\mathbf{z}). \quad (23)$$

If we limit ourselves to the ensemble of reactive trajectories and ask what is the probability density of finding them at \mathbf{z} (i.e., we look at the probability density of finding a trajectory at \mathbf{z} conditional on it being reactive), we need to normalize ρ_R , i.e.,

$$\hat{\rho}_R(\mathbf{z}) = Z_R^{-1} q_+(\mathbf{z})q_-(\mathbf{z})\rho(\mathbf{z}), \quad (24)$$

where the normalization factor

$$Z_R = \int_{\Omega} q_+(\mathbf{z})q_-(\mathbf{z})\rho(\mathbf{z})d\mathbf{z} \quad (25)$$

is the probability of being A - B reactive. The formula above was first derived (29) as a way to analyze the transition-path ensemble sampled by TPS.

Figure 5 shows the isosurfaces of $\hat{\rho}_R$ in the example of the rugged Mueller potential. Not surprisingly, this density is also rugged and is peaked in the shallow region between A and B because this region is a dynamical trap for the transition. This example shows that the information given by $\hat{\rho}_R$ about the mechanism of the reaction is somewhat limited, and the object most useful for characterizing the reaction mechanism is the probability current of the reactive trajectories. We note in particular that $\hat{\rho}_R$ does not peak in the transition-state region.

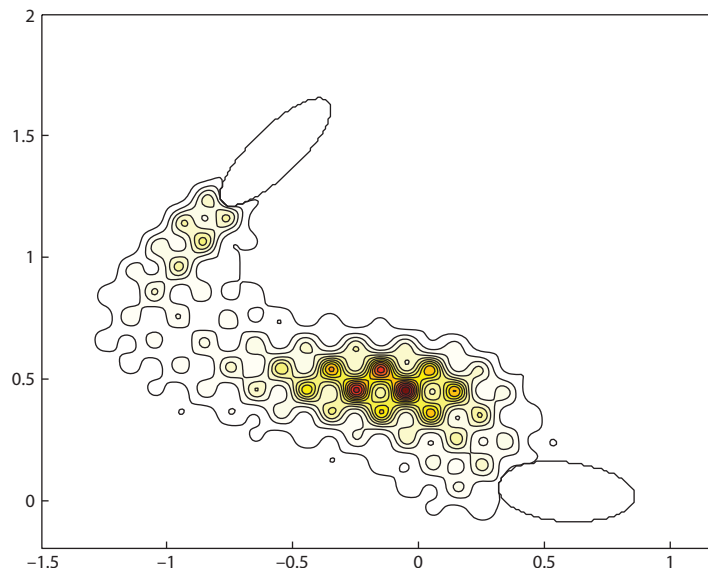


Figure 5

Contour lines of the probability density of reactive trajectories $\hat{\rho}_R$ for the example of the rugged Mueller potential (compare with **Figure 6**).

2.5. The Current of *A-B* Reactive Trajectories

The current of reactive trajectories can be computed directly from Equation 12 (see 8 for details):

$$\mathbf{J}_R = q_+ q_- \mathbf{J} + \rho q_- a \nabla q_+ - \rho q_+ a \nabla q_-, \quad (26)$$

where \mathbf{J} is given in Equation 13. $\nabla \cdot \mathbf{J}_R = 0$ outside of *A* and *B*, consistent with the fact that there are no other sources or sinks of reactive trajectories besides *A* and *B*. For the Langevin equation (Equation 1), Equation 26 reduces to

$$\mathbf{J}_R = Z_H^{-1} e^{-\beta H} q_+ q_- \begin{pmatrix} p \\ -\nabla U \end{pmatrix} + k_B T \gamma Z_H^{-1} e^{-\beta H} \begin{pmatrix} 0 \\ q_- \frac{\partial q_+}{\partial \mathbf{p}} - q_+ \frac{\partial q_-}{\partial \mathbf{p}} \end{pmatrix}, \quad (27)$$

where $q_-(\mathbf{x}, \mathbf{p}) = 1 - q_+(\mathbf{x}, -\mathbf{p})$. For the overdamped equation (Equation 4), we have simply

$$\mathbf{J}_R = k_B T \gamma^{-1} Z^{-1} e^{-\beta U} m^{-1} \nabla q. \quad (28)$$

The probability current \mathbf{J}_R can be analyzed in various ways. Of special interest are the flow lines of this current, i.e., the solutions of the artificial dynamics

$$\frac{d\mathbf{z}(\tau)}{d\tau} = \mathbf{J}_R(\mathbf{z}(\tau)). \quad (29)$$

If we solve this equation with initial conditions $\mathbf{z}(0)$ on the boundary of *A*, then each solution travels toward and eventually reaches *B*. The set of all these solutions are the flow lines of \mathbf{J}_R , and they indicate how the reactive trajectories proceed on average to go from *A* to *B*. Each flow line also can be weighted according to the probability flux that it carries. For instance, we can assign as weight the amplitude of the current normal to a given dividing surface *S*, i.e., a hypersurface in Ω that separates *A* and *B*. **Figure 6** shows the results of this procedure for the rugged Mueller potential, using the isocommittor surface $\{\mathbf{x} : q_+(\mathbf{x}) = \frac{1}{2}\}$ as the dividing surface. This procedure can be used to define the transition tube, a key object to which we return in Section 3. The integral

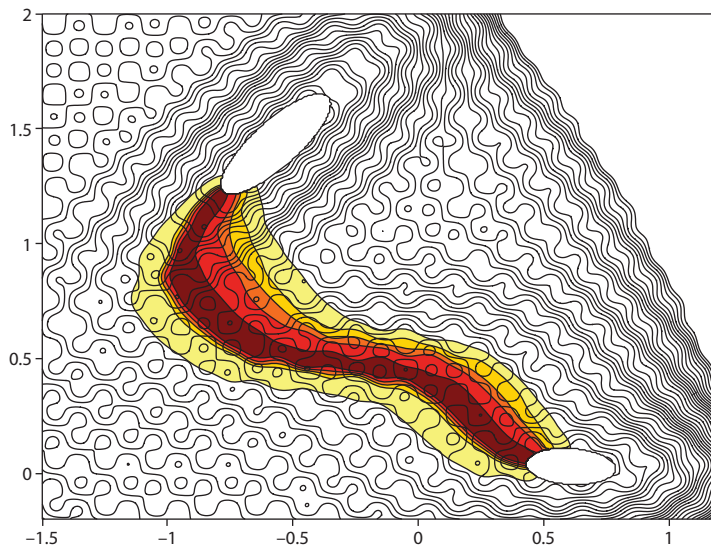


Figure 6

The flow lines of the probability current of the reactive trajectories for the example of the rugged Mueller potential. Each flow line is weighted by the amplitude of the current through the isocommittor 1/2 surface: The darker the line is, the higher this amplitude. Thus, the darker the region is, the more flux of reactive trajectories goes through the region. This permits the definition of transition tubes carrying a certain percentage of the flux of reactive trajectories. By looking at the reaction this way, the effect of the dynamical trap that influenced the probability density of reactive trajectories (see **Figure 5**) has been filtered out, and the flow lines move smoothly through this trap.

of the current through a dividing surface gives the total probability flux through this surface, i.e., the reaction rate ν_R (discussed in Section 2.6).

2.6. The Transition Rates

We let S be any dividing surface. Then by definition

$$\nu_R = \int_S \hat{n}_S(\mathbf{z}) \cdot \mathbf{J}_R(\mathbf{z}) d\sigma_S(\mathbf{z}). \quad (30)$$

REACTIVE TRAJECTORIES VERSUS FLOW LINES

The flow lines of the probability current of reactive trajectories should not be confused with the reactive trajectories themselves. Whereas the latter are random and typically quite complicated, the former are averaged objects in which all unnecessary details about the reaction have been filtered out. For instance, if there are dead ends along the way between the sets A and B or dynamical traps, the reactive trajectories will wander back and forth or get stuck in them for long periods of time. Yet these processes do not contribute much to the current nor its flow lines. This is why looking at the flow lines of the current of reactive trajectories rather than the reactive trajectories themselves is a much better way to characterize the mechanism of the reaction. This point is illustrated in **Figure 1**.

As \mathbf{J}_R is divergence-free, it is easy to see that the integral over S defined above is actually independent of S . In fact, one can show that

$$v_R = \int_{\Omega} \sum_{i,j=1}^d a_{i,j}(\mathbf{z}) \frac{\partial q_+(\mathbf{z})}{\partial z_i} \frac{\partial q_+(\mathbf{z})}{\partial z_j} \rho(\mathbf{z}) d\mathbf{z}. \quad (31)$$

For the Langevin equation (Equation 1), this is

$$v_R = k_B T \gamma Z_H^{-1} \int \sum_{i=1}^d m_i \left(\frac{\partial q_+}{\partial p_i} \right)^2 e^{-\beta H(\mathbf{x}, \mathbf{p})} d\mathbf{x} d\mathbf{p}, \quad (32)$$

and for the overdamped equation

$$v_R = k_B T \gamma^{-1} Z^{-1} \int \sum_{i=1}^d m_i \left(\frac{\partial q_+}{\partial x_i} \right)^2 e^{-\beta U(\mathbf{x})} d\mathbf{x}. \quad (33)$$

Let us now consider the rates $k_{A,B}$ and $k_{B,A}$ defined in Equation 17. These rates can be expressed as

$$k_{A,B} = \frac{v_R}{\rho_A}, \quad k_{B,A} = \frac{v_R}{\rho_B}, \quad (34)$$

where ρ_A and ρ_B are defined as

$$\rho_A = \lim_{T \rightarrow \infty} \frac{T_A}{T}, \quad \rho_B = \lim_{T \rightarrow \infty} \frac{T_B}{T} = 1 - \rho_A. \quad (35)$$

The time t contributes to T_A if, at that time, the trajectory visited A rather than B last; hence we have

$$\rho_A = \int_{\Omega} \rho(\mathbf{z}) q_-(\mathbf{z}) d\mathbf{z}, \quad \rho_B = \int_{\Omega} \rho(\mathbf{z}) (1 - q_-(\mathbf{z})) d\mathbf{z}. \quad (36)$$

2.7. Generalization: Discrete Transition-Path Theory

It is straightforward to generalize TPT to discrete systems whose dynamics is described by a discrete- or a continuous-time Markov chain. This generalization was done in Reference 14 (see also 30, 31), and it is the framework used to analyze the maze example shown in **Figure 1**. Discrete TPT is also the tool of choice for analyzing Markov state models, which have recently become popular in postprocessing long molecular dynamics (MD) simulation data (32–41). In particular, like its continuous counterpart, discrete TPT gives expressions for the probability density and current of the reactive path and thereby permits the calculation of the equivalent of the flow lines of the current of reactive trajectories, as well as the rate of the reaction (see 8, 14 for details).

2.8. Connection with Transition-State Theory

The connection with TST is most clearly seen when $\sigma^T \hat{n}_S = 0$. In this case, we have

$$\hat{n}_S \cdot \mathbf{J}_R = q_+ q_- \hat{n}_S \cdot \mathbf{J} = q_+ q_- \hat{n}_S \cdot \tilde{\mathbf{b}} \rho, \quad (37)$$

where $\tilde{\mathbf{b}}(\mathbf{z})$ is given by

$$\tilde{b}_i(\mathbf{z}) = b_i(\mathbf{z}) + \sum_{j,k=1}^d \frac{\partial \sigma_{i,k}(\mathbf{z})}{\partial z_j} \sigma_{j,k}(\mathbf{z}). \quad (38)$$

As a result

$$v_R = \int_S \tilde{\mathbf{b}}(\mathbf{z}) \cdot \hat{n}_S(\mathbf{z}) q_+(\mathbf{z}) q_-(\mathbf{z}) \rho(\mathbf{z}) d\sigma_S(\mathbf{z}). \quad (39)$$

Conversely, it can be shown that the TST rate is in this case given by

$$v_{\text{TST}} = \int_S (\tilde{\mathbf{b}}(\mathbf{z}) \cdot \hat{\mathbf{n}}_S(\mathbf{z}))_+ \rho(\mathbf{z}) d\sigma_S(\mathbf{z}), \quad (40)$$

where $(\tilde{\mathbf{b}} \cdot \nabla \theta)_+ = \max(\tilde{\mathbf{b}} \cdot \nabla \theta, 0)$ (42, 43). In the case of the Langevin equation (Equation 1), Equation 40 reduces to

$$v_{\text{TST}} = \sqrt{\frac{k_B T}{2\pi}} Z^{-1} \int_S |m^{-1/2} \mathbf{n}_S(\mathbf{x})| e^{-\beta U(\mathbf{x})} d\sigma_S(\mathbf{x}). \quad (41)$$

The difference between Equations 39 and 40 is that v_{TST} counts all the one-sided crossing events of the surface S , whereas v_R only counts one per transition from A to B . Therefore, $v_{\text{TST}} \geq v_R$ because every transition from A to B is associated with at least one one-sided crossing of S , but not every crossing of S leads to a transition from A to B . The ratio v_R/v_{TST} is called the transmission coefficient of the dividing surface S .

We note that, unlike TPT, TST gives no information about the reaction other than its rate.

3. ASYMPTOTIC SOLUTIONS BASED ON TRANSITION-PATH THEORY

3.1. Transition Tubes

In TPT, the committor functions are the key objects that characterize the mechanism of a reaction because they determine both the probability density and the current of reactive trajectories. A main issue then is how to find these functions and their gradients in systems of actual interest. As mentioned in Section 2.3, the main difficulty stems from the high dimensionality typical of such systems; therefore, standard numerical methods, such as finite difference or finite element, are ineffective. Here we discuss one possible way of approximating the committor function, which is the basis of the string method discussed in Sections 4 and 5.

For simplicity, we discuss first the case of the overdamped dynamics:

$$\dot{\mathbf{x}} = -\nabla U(\mathbf{x}) + \sqrt{2k_B T} \dot{\mathbf{w}}(t). \quad (42)$$

The committor functions associated with Equation 42 are such that $q_+(\mathbf{x}) = q(\mathbf{x})$ and $q_-(\mathbf{x}) = 1 - q(\mathbf{x})$, where $q(\mathbf{x})$ satisfies

$$\begin{cases} -\nabla U \cdot \nabla q + k_B T \Delta q = 0, & \mathbf{x} \notin A \cup B, \\ q = 0, & \mathbf{x} \in A, \\ q = 1, & \mathbf{x} \in B. \end{cases} \quad (43)$$

To proceed, we make the assumption that most of the flux of reactive trajectories goes through one or a few isolated and localized tubes. Instead of solving Equation 43 to find q everywhere, it is only necessary to find q inside these tubes. As shown below, this approximation drastically reduces the complexity of the problem.

To avoid confusion, we stress that the localized tube assumption is about the flux of reactive trajectories, not the reactive trajectories themselves: The flux may very well be localized in a few tubes even in situations in which the reactive trajectories are not (e.g., see **Figure 1**).

3.1.1. Defining transition tubes via the flux density across the isocommittor surfaces. The current of reactive trajectories associated with Equation 42 is

$$\mathbf{J}_R(\mathbf{x}) = Z^{-1} e^{-\beta U(\mathbf{x})} \nabla q(\mathbf{x}). \quad (44)$$

Let us suppose that we look at the flux induced by this current through a given set of surfaces that foliate the space between A and B , i.e., such that they each are a dividing surface, they do not intersect, and their union is the region between A and B . In addition, let us suppose that there exist regions where this flux is localized on each surface (e.g., carrying a certain percentage of the total flux through each surface). Then the ensemble of these regions forms a few tubes carrying this percentage of the flux of reaction trajectories.

Which surfaces should we use in this construction? The correct ones are the isocommittor surfaces $\{q(\mathbf{x}) = q^*\}$ with $q^* \in [0, 1]$. These surfaces form a foliation. In addition, they have the remarkable property that the flux intensity through these surfaces, i.e., $j_R(\mathbf{x}) = \hat{\mathbf{n}} \cdot \mathbf{J}_R = \nabla q \cdot \mathbf{J}_R / |\nabla q|$ or explicitly from Equation 44

$$j_R(\mathbf{x}) = Z^{-1} e^{-\beta U(\mathbf{x})} |\nabla q(\mathbf{x})|, \quad (45)$$

is proportional to the probability density of the last hitting point of the reactive trajectories on the surface. This property was established in Reference 44 and it is discussed further in Reference 8.

3.1.2. Approximations of the committor function. If we connect the center of the regions where a transition tube intersects the isocommittor surfaces, this defines a curve γ . Let us parametrize the points along this curve by $\varphi(s)$ with $s \in [0, L]$. Here s is the arc length along γ and L is the length of this curve so that $|\varphi'(s)| = 1$ (below, for convenience, we use other parameterizations, e.g., based on normalized arc length, but this one is simpler for the calculations in this section). Given \mathbf{x} , we let $s(\mathbf{x})$ be the parameter such that $\varphi(s(\mathbf{x}))$ is the point along γ closest to \mathbf{x} (see **Figure 7**). We look for approximation of q under the assumption

$$q(\mathbf{x}) = f(s(\mathbf{x})). \quad (46)$$

In other words, the function $f: [0, L] \rightarrow [0, 1]$ specifies the value of $q(\mathbf{x})$ along the curve, and the value of $q(\mathbf{x})$ at any point \mathbf{x} not on the curve is the same as the one at the point on the curve closest to \mathbf{x} , $\varphi(s(\mathbf{x}))$. Equation 46 implies that the isosurfaces of $q(\mathbf{x})$ are the same as the ones of $s(\mathbf{x})$, up to relabeling, and it is supposed to hold only in the transition tube, i.e., only locally in the vicinity of the curve γ . The problem is now reduced to finding the curve γ , on which we focus below.

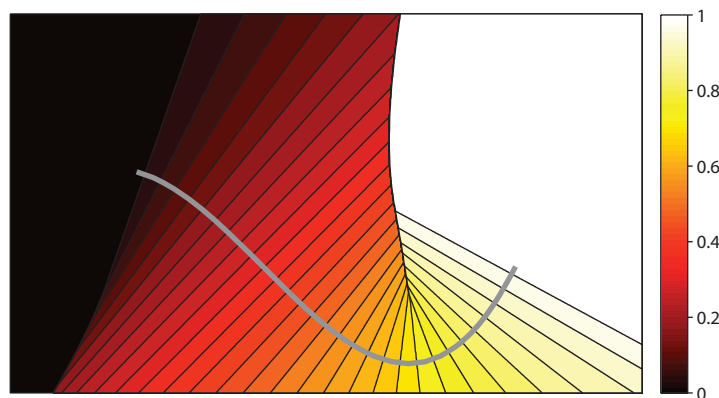


Figure 7

Contour lines of the function $s(\mathbf{x})$ associated with the unit length ($L = 1$) curve shown in gray. The ansatz in Equation 46 amounts to the assumption that locally around such a curve the isosurfaces of $s(\mathbf{x})$ and those of $q(\mathbf{x})$ coincide.

3.2. The Minimum Energy Path

In this section we assume that there exists one (or more generally a few) line of current γ that carries most of the flux of reactive trajectories (i.e., the transition tubes are thin). Then, following the construction outlined in Section 3.1, this line of current must be such that it maximizes $j_R(\mathbf{x})$ in each isosurface of $q(\mathbf{x})$. Using the ansatz (Equation 46), which implies that $\nabla q(\mathbf{x}) = f'(s(\mathbf{x}))\nabla s(\mathbf{x})$, from Equation 45 this is equivalent to the requirement that, in $s(\mathbf{x}) = s$, $Z^{-1}e^{-\beta U(\mathbf{x})}f'(s)|\nabla s(\mathbf{x})|$ must be maximum at $\mathbf{x} = \varphi(s)$. This also means that the gradient of $j_R(\mathbf{x})$ must be parallel to $\nabla s(\mathbf{x})$ along γ , i.e.,

$$\nabla (e^{-\beta U(\varphi)}|\nabla s(\varphi)|) \text{ must be parallel to } \nabla s(\varphi) \text{ along } \gamma, \quad (47)$$

neglecting factors that are constants in $s(\mathbf{x}) = s$. After some manipulations using the definition of $s(\mathbf{x})$, we arrive at

$$-\beta[\nabla U]^\perp + \varphi'' = 0, \quad (48)$$

where $[\nabla U]^\perp = \nabla U - (\nabla U \cdot \varphi')\varphi'$ is the component of ∇U perpendicular to γ and we use $[\varphi'']^\perp = \varphi''$ (see 8 for details). Equation 48 is the well-known equation for the path of max flux originally derived in Reference 46 using a different approach. If most of the flux of reactive trajectory is indeed carried by the flow line satisfying Equation 48, the term φ'' is a small correction compared to $-\beta[\nabla U]^\perp$, and therefore Equation 48 can be approximated by

$$[\nabla U]^\perp = 0, \quad (49)$$

which is the well-known equation for the MEP. Written in the original, non-mass-weighted coordinates, Equations 48 and 49 read, respectively,

$$-\beta[m^{-1}\nabla U]^\perp + \frac{\varphi''}{|m^{1/2}\varphi'|^2} = 0 \quad (50)$$

and

$$[m^{-1}\nabla U]^\perp = 0. \quad (51)$$

What about the function f ? If we compute the rate v_R for the isocommittor surface $q(\mathbf{x}) = f(s)$, we obtain

$$v_R = k_B T f'(s) e^{-\beta F(s)}, \quad (52)$$

where we define the free energy of $s(\mathbf{x})$

$$F(s) = -k_B T \ln \int Z^{-1} e^{-\beta U(\mathbf{x})} \delta(s(\mathbf{x}) - s) d\mathbf{x}. \quad (53)$$

Because v_R is independent of s , and because $f(0) = 0, f(L) = 1$, we have

$$f(s) = \frac{\int_0^s e^{\beta F(s')} ds'}{\int_0^L e^{\beta F(s')} ds'}. \quad (54)$$

Inserting this expression back into Equation 52, we get

$$v_R = k_B T \left(\int_0^L e^{\beta F(s')} ds' \right)^{-1}. \quad (55)$$

In terms of the non-mass-weighted coordinates and the original units of time, Equation 53 remains valid, but Equation 54 must be replaced by

$$f(s) = \frac{\int_0^s |m^{1/2}\varphi'(s')|^2 e^{\beta F(s')} ds'}{\int_0^L |m^{1/2}\varphi'(s')|^2 e^{\beta F(s')} ds'}, \quad (56)$$

and Equation 55 must be replaced by

$$\nu_R = k_B T \gamma^{-1} \left(\int_0^L |m^{1/2} \varphi'(s')|^2 e^{\beta F(s')} ds' \right)^{-1}. \quad (57)$$

The free energy $F(s)$ can be computed within the context of the finite-temperature string method (see Section 5.1).

3.3. Connection with Variational Transition-State Theory

We recall that for Langevin dynamics, the TST rate is given by Equation 41, in which the dividing surface is arbitrary. As explained in Section 2.8, because ν_{TST} gives an upper bound on the actual reaction rate ν_R , it is natural to optimize the dividing surface so as to minimize the TST rate. This is referred to as variational TST, and it amounts to viewing Equation 41 as an objective function to be minimized over all possible dividing surfaces. The Euler-Lagrange equation for this minimization problem can be written down explicitly (2, 43) (for simplicity, we return to mass-weighted coordinates),

$$-\beta \nabla U \cdot \hat{n}_S + \kappa_S = 0, \quad (58)$$

where \hat{n}_S is the unit normal to the surface and $\kappa_S = \nabla \cdot \hat{n}_S$ its local curvature, and we must look for a solution that leaves the reactant set on one side and the product set on the other. Equation 58 is complicated, but it becomes much simpler if we assume that the curvature term is small and can be neglected. In this case, Equation 58 reduces to

$$\nabla U \cdot \hat{n}_S = 0. \quad (59)$$

The solutions are the stable manifold of any saddle point, i.e., the set of all initial conditions such that the solutions of $\dot{\mathbf{x}} = -\nabla U(\mathbf{x})$ converge to the saddle point as $t \rightarrow \infty$. This set forms a dividing surface and illustrates why the MEP is relevant also in the context of variational TST. Indeed, having identified a MEP between two minima, we can localize the saddle point along it, and thereby calculate at least locally (e.g., by using a planar approximation) the optimal dividing surface according to Equation 59.

Even the TST rate associated with the optimal dividing surface may be a poor approximation of ν_R if there are substantial recrossings. These problems are overcome in TPT because it considers a family of isocommittor surfaces that foliates the configuration (or phase) space between the reactant and product sets, not just a single dividing surface.

3.4. Working with Collective Variables: The Minimum Free Energy Path

As discussed in Section 3.2, a difficulty in realistic examples is the typical ruggedness of their potential energy surfaces, and when that is the case, it becomes inappropriate to look for most probable transition paths. One way around this problem is to introduce some appropriate collective variables (i.e., a set of functions of the Cartesian coordinates of the system such as dihedral angles and bond distances) and try to reformulate the problem in terms of these variables rather than the original ones. This amounts to analyzing the reaction using the free energy landscape associated with the collective variables rather than the original energy landscape $U(\mathbf{x})$. If the collective variables are chosen well (which is a nontrivial issue), we may expect that the free energy landscape will be smooth even if $U(\mathbf{x})$ is rugged, and entropic effects will be less of an issue as well. There is an obvious similarity to the notion of reaction coordinates that are commonly used in the literature. Here we use the term collective variables for the main reason that the term reaction

coordinates is by now a much abused terminology that should be reserved for objects such as the committor function, which is the single quantity needed to explain the reaction, whereas collective variables are those used to parameterize the committor function and can live in rather high dimensions (the relevant formalism can be found in 8 and 19). In particular, what replaces the MEP is the minimum free energy path (MFEP).

One should not confuse the concept of slow variables of a dynamical system with the collective variables that we use here. In particular, the slow variables are not necessarily a good set of collective variables. An explicit example can be found in the Reference 8.

3.5. The Case of the Langevin Equation

Generalizing the ideas of the previous sections to the Langevin equation (Equation 1) poses an additional difficulty, namely that the equivalent of the objective function (Equation 20) does not exist for $q_+(\mathbf{x}, \mathbf{p})$. This is related to the fact that, unlike the overdamped dynamics, the Langevin dynamics is not statistically invariant under time reversal (invariance requires also a flip of the momenta). We can bypass this difficulty by replacing Equation 20 with the following the least-squares principle in which we minimize

$$\tilde{I}(q_+) = Z_H^{-1} \int |Lq_+|^2 e^{-\beta H(\mathbf{x}, \mathbf{p})} d\mathbf{x} d\mathbf{p}, \quad (60)$$

where L is the generator of the Langevin equation:

$$Lq_+ = m^{-1} \mathbf{p} \cdot \nabla_{\mathbf{x}} q_+ - \nabla U \cdot \nabla_{\mathbf{p}} q_+ - \gamma \mathbf{p} \cdot \nabla_{\mathbf{p}} q_+ + \gamma k_B T m : \nabla_{\mathbf{p}} \nabla_{\mathbf{p}} q_+. \quad (61)$$

Clearly, the solution of $Lq_+ = 0$ is a minimizer of \tilde{I} . Equation 60 can be used as the starting point for further approximations. One such approximation is based on the assumption that the committor function $q_+(\mathbf{x}, \mathbf{p})$ can be represented by a function of the positions only, i.e.,

$$q_+(\mathbf{x}, \mathbf{p}) \approx q(\mathbf{x}) = \langle q_+(\mathbf{x}, \mathbf{p}) \rangle_{\mathbf{p}}. \quad (62)$$

If one inserts this ansatz into Equation 60 and performs explicitly the integration over the momenta, it is easy to see that $\tilde{I}(q)$ reduces exactly to the objective function (Equation 20) that arises in the context of the overdamped equation (Equation 4). As discussed in Section 3.4, this does not mean that the overdamped equation necessarily captures the actual dynamics of the system, but it can be used to explain the mechanism of the reaction if one assumes that Equation 62 holds. Under this assumption, we can use all the technology discussed in Sections 3.2–3.4 to analyze the reaction via the identification of either the MEPs or MFEPs. Under this assumption, we can also use the procedure explained in Section 3.6 when neither the MEP nor the MFEP is the relevant object.

3.6. Going Beyond the Thin Tube Assumption via Principal Curves

One difficulty with the MEP is that it gives a viewpoint on the reaction that is too local. Indeed, by trying to identify a single line of current that carries most of the flux of reactive trajectories, one ignores transition channels that are less favorable energetically, but are broader and may indeed carry more flux. The same criticism may apply to the MFEP, although to a lesser extent.

To go beyond the concepts of MEP or MFEP, we must look at the problem more globally. Instead of trying to identify the point that maximizes the current intensity on each isocommittor surface (as done in Section 3.2 to get the MEP), one possibility (advocated in 17, 18, 21, 22, 47) is to look for the position in these surfaces that is centroidal with respect to the current intensity

$j_R(\mathbf{x})$ defined in Equation 45. In other words, assuming that Equation 46 holds, we can look for $\varphi(s)$ that solves for every $s \in [0, L]$

$$0 = \int_{s(\mathbf{x})=s} (\mathbf{x} - \varphi(s)) j_R(\mathbf{x}) d\sigma(\mathbf{x}) \\ \equiv Z^{-1} f'(s) \int_{s(\mathbf{x})=s} e^{-\beta U(\mathbf{x})} |\nabla s(\mathbf{x})|^2 d(s(\mathbf{x}) - s) d\mathbf{x}, \quad (63)$$

where $d\sigma(\mathbf{x})$ denotes the surface element in $s(\mathbf{x}) = s$, and we use $|\nabla q| = f'(s)|\nabla s|$. If we neglect curvature effects and approximate $|\nabla s|$ by its value $|\varphi'| = 1$ along the curve, up to an irrelevant proportionality factor, Equation 63 reduces to the following equation for $\varphi(s)$:

$$0 = \int (\mathbf{x} - \varphi(s)) e^{-\beta U(\mathbf{x})} \delta(s(\mathbf{x}) - s) d\mathbf{x}, \quad (64)$$

which means that the conditional canonical expectation of \mathbf{x} in $s(\mathbf{x}) = s$ must be $\varphi(s)$ for every $s \in [0, L]$, i.e.,

$$\varphi(s) = \langle \mathbf{x} \rangle_{s(\mathbf{x})=s}. \quad (65)$$

The curve satisfying this requirement is an object, familiar in the statistics literature (48, 49), called the principal curve associated with the density $Z^{-1}e^{-\beta U(\mathbf{x})}$. Its main advantage over the MEP is that it permits one to look more globally at the flux going through each isocommittor surface. Indeed, the principal curve γ identified via Equation 65 is not meant to be a single line of current that carries most of the flux, but rather is the center of a tube carrying most of the flux, and its location is influenced by the width of the tube. Because Equation 65 also involves an average in each isocommittor surface, this smoothes out irrelevant details on the thermal scale or below in these surfaces and makes the curve γ less sensitive to these details. **Figure 8** illustrates this in

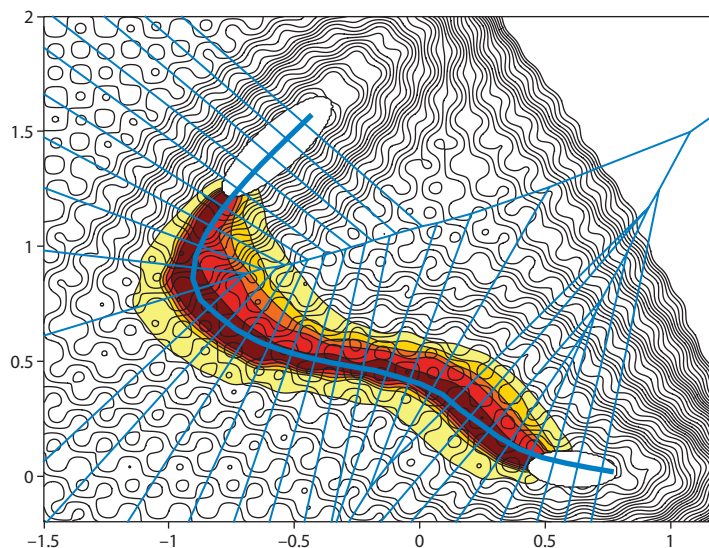


Figure 8

The principal curve solution of Equation 64 for the example of the rugged Mueller potential. Also shown are the contour lines of the function $s(\mathbf{x})$ associated with the curve, and, in the background, the actual current of reactive trajectories already shown in **Figure 6**. The principal curve is at the center of the tube carrying most of the flux of reactive trajectories. Inside this tube, the isosurfaces of the function $s(\mathbf{x})$ are good approximations of the isocommittor surfaces, i.e., $q(\mathbf{x}) \approx f(s(\mathbf{x}))$, with f given in Equation 54. Also, the principal curve is rather smooth; i.e., it is not affected much by the ruggedness of the potential.

the context of the rugged Mueller potential. Under the assumptions above, Equation 54 for the function f remains valid.

We can include the next order term in Equation 65 by using $|\nabla s|^2 \approx 1 - 2\boldsymbol{\varphi}'' \cdot (\mathbf{x} - \boldsymbol{\varphi})$. It is easy to see that using this approximation in Equation 63 gives the equation

$$0 = \langle \mathbf{x} \rangle_{s(\mathbf{x})=s} - \boldsymbol{\varphi}(s) + C(s)\boldsymbol{\varphi}''(s), \quad (66)$$

where we define the tensor

$$C(s) = 2\langle (\mathbf{x} - \boldsymbol{\varphi})(\mathbf{x} - \boldsymbol{\varphi})^T \rangle_{s(\mathbf{x})=s}. \quad (67)$$

Equation 66 is to Equation 65 what the equation for the line of max flux (Equation 48) is to the equation for the MEP (Equation 49).

Numerical algorithms for solving Equations 65 and 66 are presented in Section 5. These equations can also be generalized in collective variable space by an appropriate change of metric (8).

4. NUMERICAL ALGORITHMS FOR COMPUTING THE MINIMUM ENERGY PATH

For systems with smooth energy landscapes for which the original TST or Kramers rate theory gives a sufficiently accurate description of the transition process, the main objects of interest are the transition states, which are saddle points on the potential energy landscape. From a numerical viewpoint, we are naturally interested in algorithms for finding such saddle points. Ideas such as Newton's method (50), the dimer method (51), and conjugate peak refinement (52) are developed for this purpose. These algorithms are intended for searching the saddle points directly. However, in cases in which the initial and final states are separated by intermediate stable states, one is interested in a sequence of transition states. In that case, algorithms for finding saddle points are no longer sufficient for determining the relevant sequence of transition states. Instead, one must look for the MEP.

In this section, we mostly focus our discussion on the (zero-temperature) string method. Even though it shares many similarities with several other strategies developed earlier (particularly after discretization), the string method distinguishes itself by two important features that are worth mentioning.

First, as we discussed in Section 3.2, the MEP is defined as a curve in configuration space. Therefore, to look for the MEP, it is most natural to use an algorithm that moves curves in the configuration space. The string method does exactly that: It is an intrinsic formulation of the dynamics of curves in the configuration space. This contrasts with algorithms that are formulated as chain of states in the first place. After discretizing the curves, the string method also resembles a chain-of-states method. Nevertheless, it is much better to start with an intrinsic formulation and then discretize. After all, this is why calculus is so important and useful. In addition, because the states are continuously being reinterpolated, the states in the string method do not have the fixed identity that other chain-of-states methods have.

Second, the intrinsic formulation offers practical advantages. One is that it is much easier to be extended to the case with rough energy landscapes (the finite-temperature string method). Another is that it is much easier to improve the accuracy of the algorithms that are based on an intrinsic formulation.

For simplicity, throughout this section we use mass-weighted coordinates. The formulas below translated back into the original coordinates can be found in Reference 8.

4.1. The Zero-Temperature String Method

One main motivation for the string method is to formulate a strategy based on the intrinsic dynamics of curves connecting two local minima of the potential $U(\mathbf{x})$ located, for example, at \mathbf{x}_a and \mathbf{x}_b . The dynamics of curves is determined by the normal velocity at each point along the curve. The tangential component does not affect the graph of the curve. Because the MEP satisfies Equation 51, the simplest dynamics for the evolution of the curve toward a MEP is given abstractly by

$$\mathbf{v}_n = -[\nabla U]^\perp, \quad (68)$$

where \mathbf{v}_n denotes the normal velocity of the curve. This formulation guarantees that it is gauge invariant; i.e., it is invariant under the change of the parameterization of the curve.

To translate Equation 68 into a form that can be readily used in numerical computations, we assume that we have picked a particular parameterization of the evolving curve, $\gamma(t)$. For numerical purposes, the simplest choice is to use equal-arc-length parameterization. In this case the curve $\gamma(t)$ is represented as $\gamma(t) = \{\varphi(\alpha, t) : \alpha \in [0, 1]\}$, where α is a constant multiple of the arc length from $\varphi(0, t)$ to the point $\varphi(\alpha, t)$.² We denote using a prime the derivative with respect to α , and we then have $|\varphi'| = \text{constant}$ in α [this constant is the length of the curve $\gamma(t)$]. Other parameterizations are possible as well. For instance, we can add an energy-dependent weight function along the curve to enhance the accuracy near the saddle points (16). In this case, $w(\alpha)|\varphi'(\alpha, t)| = \text{constant}$ in α , where $w(\alpha)$ is the weight function. This idea has been used quite extensively since the 1980s, for example, in Brower et al.'s work (53, 54) on geometric models of interface evolution.

Two slightly different forms of the string method have been suggested (16, 55). The original form was based on the evolution equation

$$\dot{\varphi} = -[\nabla U(\varphi)]^\perp + \lambda \hat{\tau}, \quad (69)$$

which is just the parametric version of Equation 68: $\dot{\varphi}$ denotes the time derivative of φ , $\hat{\tau} = \varphi'/|\varphi'|$ is the unit tangent vector along the string, and $\lambda \hat{\tau}$ is a Lagrange multiplier term for the purpose of enforcing the particular parameterization of the string, such as the equal-arc-length parameterization. The action of this term is easy to compute and amounts to a reparameterization step, as explained below. There is, however, a subtle point associated with the discretization of Equation 69 related to the fact that the component of $-\nabla U(\varphi)^\perp$ parallel to $\hat{\tau}$ is a convection term that needs to be discretized carefully to avoid numerical instabilities (16, 56), which has been previously noted (57). Conversely, because the component of $-\nabla U(\varphi)^\perp$ parallel to $\hat{\tau}$ can be absorbed into the Lagrange multiplier term, Equation 69 can be recast into

$$\dot{\varphi} = -\nabla U(\varphi) + \bar{\lambda} \hat{\tau}, \quad (70)$$

where the particular parameterization of the string is now enforced by the action of $\bar{\lambda} \hat{\tau}$. This new form permits us to eliminate the numerical instability issue discussed above.

In actual computations, the string is discretized into a number of images $\{\varphi_i(t), i = 0, 1, \dots, N\}$, where $\varphi_i(t) = \varphi(\alpha = i/N, t)$. The images along the string are evolved by iterating upon the following two-step procedure.

1. Evolution step. The images on the string are evolved over some time interval Δt according to the potential force at that point:

$$\dot{\varphi}_i = -\nabla U(\varphi_i). \quad (71)$$

²We use a constant multiple of the arc length, instead of the arc length itself as in Section 3.1, so that the range of the parameter α is fixed, $\alpha \in [0, 1]$, even if the length of the curve $\gamma(t)$ varies during its evolution. This is more convenient in the numerics.

This equation can be integrated in time by any stable ordinary differential equation (ODE) solver (e.g., the forward Euler method or Runge-Kutta methods).

2. Reparameterization step. The points (images) are redistributed along the string using a simple interpolation procedure (see 55). In the example of equal-arc-length parameterization, the reparameterization step again involves two steps. The first step is to compute the arc-length function along the string, i.e., the piecewise linear function $\ell(\alpha)$ whose values at $\alpha = i/N$ are given by

$$\ell(0) = 0, \quad \ell(i/N) = \sum_{j=1}^i |\varphi_j - \varphi_{j-1}|, \quad i = 1, \dots, N. \quad (72)$$

This allows us to compute the new parameterization, the values of $\{\alpha_i, i = 0, 1, \dots, N\}$, which compose an equal-distance parameterization, i.e.,

$$\ell(\alpha_i) = \frac{i}{N} \ell(1). \quad (73)$$

The second step is to compute the images at these new parameter values using standard piecewise polynomial interpolation. For instance, if one uses linear interpolation, this amounts to constructing the piecewise linear function $\varphi(\alpha)$ such that its values at $\alpha = i/N$ are the images before reparameterization, then one sets $\varphi_i = \varphi(\alpha_i)$.

The time interval Δt between the reparameterization steps can be bigger than the actual time step used to evolve Equation 71. A practical way to determine when to invoke the reparameterization procedure is to monitor the distances between neighboring points along the string by Equation 71 and then move to the reparameterization step if the ratio of the largest to the smallest distances goes above a given prescribed tolerance. Also, the position of the end points along the curve, $\varphi_0(t)$ and $\varphi_N(t)$, is not affected by the reparameterization step because $\alpha_0 = 0$ and $\alpha_N = 1$ from Equation 73. In other words, they find on their own the location of the nearest minima of $U(\mathbf{x})$ even if the end points of the curve were not initially there.

The version of the string method described above is a simple but effective technique for finding the MEPs. Its implementation requires only a simple ODE solver for the evolution step, and a simple interpolation routine for the parameterization step. It is therefore easy to use and can be readily incorporated into any existing code as long as the code provides force evaluation.

The string method can be generalized in various ways. For instance, its convergence rate can be improved by Broyden's method (16) or other quasi-Newton techniques (58), a version of the method with a growing string has been proposed (59), and it can be used in the context of ab initio calculations (60).

The string method can also be generalized to work in collective variable space and compute the MFEP rather than the MEP. This generalization was developed in References 19, 20, and 61, and it is discussed in Reference 8. Recently, several close variants of the string method in collective variable space have been proposed (45, 62–64).

4.2. Action-Based Methods for Calculating the Minimum Energy Path

As originally noted by Olender & Elber (65) and rederived in Reference 66, it is possible to write down a variational formulation for the MEP. Specifically, the MEP is the minimizer of

$$E(\varphi) = \int_0^1 |\nabla U(\varphi)| |\varphi'| d\alpha, \quad (74)$$

which suggests the possibility of identifying MEPs by solving the Euler-Lagrange equation associated with Equation 74:

$$[\nabla \nabla U \nabla U]^\perp - \frac{|\nabla U|^2}{|\varphi'|^2} \varphi'' = 0, \quad (75)$$

which can be discretized as

$$\begin{aligned} & \nabla \nabla U(\varphi_i) \nabla U(\varphi_i) - (\nabla \nabla U(\varphi_i) \nabla U(\varphi_i) \cdot \hat{\tau}_i) \hat{\tau}_i \\ & - \frac{|\nabla U(\varphi_i)|^2}{|\varphi_{i+1} - \varphi_{i-1}|^2} (\varphi_{i+1} + \varphi_{i-1} - 2\varphi_i) = 0, \quad i = 1, \dots, N-1, \end{aligned} \quad (76)$$

where $\hat{\tau}_i = (\varphi_{i+1} - \varphi_{i-1})/|\varphi_{i+1} - \varphi_{i-1}|$, and we have the boundary conditions $\varphi_0 = \mathbf{x}_a$ and $\varphi_N = \mathbf{x}_b$. This equation can then be solved, e.g., by Broyden's method (50). A disadvantage of Equation 76 is that it requires computing $\nabla \nabla U \nabla U$. In practice, this can be done via finite difference using two force evaluations per image, i.e.,

$$\nabla \nabla U(\varphi_i) \nabla U(\varphi_i) \approx \delta^{-1} [\nabla U(\varphi_i + \delta \nabla U(\varphi_i)) - \nabla U(\varphi_i)], \quad (77)$$

where δ is a small parameter. Equation 76 automatically enforces the equal-arc-length parameterization of the string. Indeed, multiplying this equation by $\hat{\tau}_i$ implies that

$$\hat{\tau}_i \cdot (\varphi_{i+1} + \varphi_{i-1} - 2\varphi_i) = 0, \quad i = 1, \dots, N-1. \quad (78)$$

This equation can be cast into

$$\frac{|\varphi_{i+1} - \varphi_i|^2 - |\varphi_i - \varphi_{i-1}|^2}{|\varphi_{i+1} - \varphi_{i-1}|} = 0, \quad i = 1, \dots, N-1; \quad (79)$$

i.e., when Equation 76 is satisfied, the images must be equidistant.

The idea discussed above can also be used to calculate the line of max-flux solution of Equation 48. Equation 48 can be discretized as

$$-\beta \nabla U(\varphi_i) + \beta (\nabla U(\varphi_i) \cdot \hat{\tau}_i) \hat{\tau}_i - \frac{\varphi_{i+1} + \varphi_{i-1} - 2\varphi_i}{|\varphi_{i+1} - \varphi_{i-1}|^2} = 0, \quad (80)$$

where $i = 1, \dots, N-1$, $\varphi_0 = \mathbf{x}_a$, and $\varphi_N = \mathbf{x}_b$. Like Equation 76, Equation 80 automatically enforces the equal-arc-length parameterization of the string. Solving Equation 80 by Broyden's method is simpler than solving Equation 76.

4.3. Chain-of-States Methods

4.3.1. Elastic-band method. The basic idea of the elastic-band method is to connect the two stable states \mathbf{x}_a and \mathbf{x}_b by a chain of states (replicas or images) and evolve this chain of states. In an early attempt, Pratt (9) proposed the use of Monte Carlo methods to sample chains of states between the initial and final states to find the transition-state region. Pratt's idea has been developed in two directions. One is Monte Carlo algorithms for sampling true dynamical trajectories between the initial and final states. This is the well-known TPS algorithm (11, 67). The second is the class of optimization algorithms for finding the MEP using a chain of states. The elastic-band method is an example of this type of algorithm.

Given a chain of states $\{\mathbf{x}_0, \mathbf{x}_1, \dots, \mathbf{x}_N\}$, where $\mathbf{x}_0 = \mathbf{x}_a$, $\mathbf{x}_N = \mathbf{x}_b$, let us define an energy for the chain:

$$E(\mathbf{x}_1, \dots, \mathbf{x}_{N-1}) = \sum_{i=1}^{N-1} U(\mathbf{x}_i) + \frac{k\Delta\alpha}{2} \sum_{i=1}^N \frac{|\mathbf{x}_i - \mathbf{x}_{i-1}|^2}{\Delta\alpha^2}, \quad (81)$$

where $\Delta\alpha = 1/N$ and $k > 0$ is a parameter. Alternative energy functions have been proposed (68, 69).

In the elastic-band method (also called the plain elastic-band method, to be contrasted with the nudged elastic-band method discussed below), the idea is to move the chain of states according to the gradient flow of the energy E (70):

$$\dot{\mathbf{x}}_i = -\frac{\partial E}{\partial \mathbf{x}_i} = -\nabla U(\mathbf{x}_i) + k \frac{\mathbf{x}_{i+1} + \mathbf{x}_{i-1} - 2\mathbf{x}_i}{\Delta\alpha}, \quad i = 1, \dots, N-1, \quad (82)$$

where the first term at the right-hand side is the potential force, and the second term is the spring force. Because of how the scaling in the coefficient of the second term is chosen, if we use an explicit ODE solver to evolve Equation 82, the time step size allowed is $\Delta t \sim \Delta\alpha$ to guarantee long-time numerical stability. However, in this scaling, the second term drops out in the continuum limit as $\Delta\alpha \rightarrow 0$.

The elastic-band method is extremely simple and intuitive. However, it fails to converge to the MEP because the spring force tends to make the chain straight, which leads to corner-cutting (70).

4.3.2. The nudged elastic-band method. To overcome the corner-cutting problem, Jónsson and colleagues (71–73) introduced the nudged elastic-band method. This is a simple modification of the elastic-band method, but one that made the method truly useful. Instead of using the total potential force and spring force to move the chain, one uses only the normal component of the potential force and the tangential component of the spring force:

$$\dot{\mathbf{x}}_i = -[\nabla U(\mathbf{x}_i)]^\perp + (F_i^s \cdot \hat{\tau}_i)\hat{\tau}_i, \quad i = 1, \dots, N-1, \quad (83)$$

where $F_i^s = k(\mathbf{x}_{i+1} + \mathbf{x}_{i-1} - 2\mathbf{x}_i)/\Delta\alpha$, and $\hat{\tau}_i$ denotes the tangent vector along the elastic band at \mathbf{x}_i .

If the chain converges to a steady state, it should be (a discretized approximation of) a MEP. In fact, from Equation 83, we see that if the left-hand side vanishes, then

$$-[\nabla U(\mathbf{x}_i)]^\perp + (F_i^s \cdot \hat{\tau}_i)\hat{\tau}_i = 0, \quad i = 1, \dots, N-1. \quad (84)$$

Because the two terms in this equation are normal to each other, each has to vanish. In particular, we have

$$[\nabla U(\mathbf{x}_i)]^\perp = 0, \quad i = 1, \dots, N-1, \quad (85)$$

which is the discretized version of Equation 49. We can also solve Equation 84 directly using accelerated methods such as Broyden's (73).

The choice of the elastic constant k is a crucial issue for the performance of the nudged elastic-band method. If k is too large, then the elastic band is too stiff, and one has to use very small time steps to solve the set of ODEs in Equation 83. If k is too small, then there is not enough force to prevent the states on the chain from moving away from the saddle point; hence the accuracy of the saddle point will be reduced. This difficulty can be alleviated by using the climbing-image version of the nudged elastic-band method (74), a strategy that can also be adapted to the string method (55).

It is natural to ask whether the elastic-band method can also be formulated in terms of the evolution of continuous curves. As we remarked above, if we use the original scaling of the spring constant, then the term that represents the elastic force disappears in the continuum limit (which suggests that the elastic term in Equation 82 is not enough to prevent the clustering of the states near the local minima as $\Delta\alpha \rightarrow 0$). To retain the spring term, one has to replace the spring constant k by $k/\Delta\alpha$. In that case, we can take the continuum limit of the (nudged) elastic-band method and

obtain

$$\dot{\varphi} = -[\nabla U(\varphi)]^\perp + k(\varphi' \cdot \hat{\tau})\hat{\tau}. \quad (86)$$

However, to evolve this dynamics, one has to use $\Delta t \sim (\Delta\alpha)^2$, and it will take many more iterations for the dynamics to converge to MEP.

5. FINDING THE TRANSITION TUBES

5.1. The Finite-Temperature String Method

Methods to solve Equation 65 and find principal curves have been developed in the statistics literature (see 49). These methods are adaptations of the expectation-maximization algorithm in which the maximization step is replaced by a relaxation step. Given the current configuration of the string, the new configuration is found through the following evolution steps.

1. Expectation step. Sample on the isosurfaces of the function $s(\mathbf{x})$ used in Equation 46, i.e., the pieces of hyperplanes normal to the current configuration of the string.
2. Relaxation step. Compute the empirical center of mass $\langle \mathbf{x} \rangle_{s(\mathbf{x})=s}$ on each hyperplane and move the string to a new configuration according to

$$\varphi^{n+1} = \varphi^n + \Delta t (\langle \mathbf{x} \rangle_{s(\mathbf{x})=s} - \varphi^n), \quad (87)$$

where φ^n denotes the current configuration of the string, and Δt is a step size.

In practice, the string is discretized into $N + 1$ images $\{\varphi_i, i = 0, 1, \dots, N\}$, and Equation 87 is used for each image along the string. It becomes the counterpart of the evolution step performed in the zero-temperature string method, whereas the reparameterization step is done as before (see Section 4.1). In the original version of the finite-temperature string method (17, 18, 21), $\langle \mathbf{x} \rangle_{s(\mathbf{x})=s}$ was estimated via constrained or restrained simulations in the hyperplanes perpendicular to the string. More recently (22), it was realized that there is a simpler way to estimate $\langle \mathbf{x} \rangle_{s(\mathbf{x})=s}$. The idea is to replace the surface $s(\mathbf{x}) = s$ associated with $\varphi(s)$ in the continuous setting by the Voronoi cell associated with image φ_i , i.e., the region of space that contains all the points that are closer to φ_i than to any other image:

$$B_i = \{\mathbf{x} : |\mathbf{x} - \varphi_i| < |\mathbf{x} - \varphi_j| \text{ for all } j \neq i\}. \quad (88)$$

The cells B_0 and B_N play a special role: They are the reactant and the product states A and B , respectively. For $i = 1, \dots, N - 1$, however, the cell B_i is just a mollified version of the surface $s(\mathbf{x}) = i/N$, and we then have

$$\langle \mathbf{x} \rangle_{s(\mathbf{x})=i/N} \approx \langle \mathbf{x} \rangle_{B_i}, \quad i = 1, \dots, N - 1, \quad (89)$$

where $\langle \mathbf{x} \rangle_{B_i}$ denotes a canonical average conditional on $\mathbf{x} \in B_i$. This conditional average can be computed by a simple modification of the MD integrator in which we add a momentum reversal rule at collision with the boundaries of cell B_i to confine the simulation inside this cell. Thus, if $(\mathbf{x}_i(t), \mathbf{p}_i(t))$ denotes the position and momentum at time t of the independent copy (or replica) of the MD system used to do the sampling in cell B_i , we set

$$(\mathbf{x}_i(t + \delta t), \mathbf{p}_i(t + \delta t)) = \begin{cases} (\mathbf{x}_i^*(t + \delta t), \mathbf{p}_i^*(t + \delta t)) & \text{if } \mathbf{x}_i^*(t + \delta t) \in B_i, \\ (\mathbf{x}_i(t), -\mathbf{p}_i(t)) & \text{if } \mathbf{x}_i^*(t + \delta t) \notin B_i, \end{cases} \quad (90)$$

where $(\mathbf{x}_i^*(t + \delta t), \mathbf{p}_i^*(t + \delta t))$ denotes the time-evolved value of $(\mathbf{x}_i(t), \mathbf{p}_i(t))$ after one standard MD step of size δt . We then have

$$\langle \mathbf{x} \rangle_{B_i} = \lim_{N \rightarrow \infty} \frac{1}{N} \sum_{k=0}^{N-1} \mathbf{x}_i^*(k\delta t) \quad (91)$$

up to small errors due to time discretization. The test made in Equation 90 is a simple distance check: Is $\mathbf{x}_i^*(t + \delta t)$ still closest to φ_i ? These MD calculations also can be performed in parallel in each cell B_i . Finally, it is not necessary to compute with high precision the average (Equation 91) at every update of the string. Rather, it is more efficient to evolve concurrently the images φ_i and the MD replicas and replace Equation 91 by a running time average (see 22 for details).

The scheme above can be generalized straightforwardly to solve Equation 66 rather than 65. This simply amounts to accounting for the action of the term $C(s)\varphi''$ in the updating rule (Equation 87). In fact, even when solving Equation 65, one typically needs to smooth the string to remove possible kinks arising from statistical errors. In effect, this amounts to adding a diffusion term to the updating rule (Equation 87), not unlike the one provided by the additional term $C(s)\varphi''$ in Equation 66, except that we then need to pick a value for $C(s)$ beforehand and keep it fixed once and for all. The results of a finite-temperature string method calculation made in the context of the rugged Mueller potential are shown in **Figure 9**. The finite-temperature string method can be easily generalized in collective variable space (22).

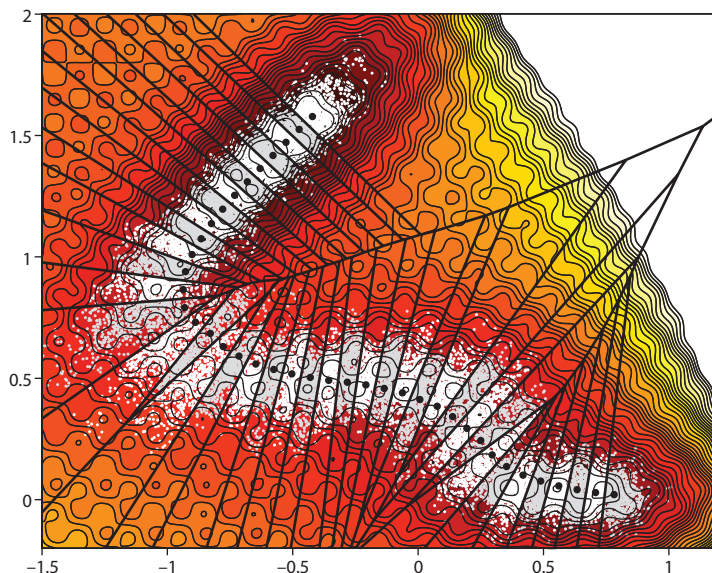


Figure 9

Results of a finite-temperature string method calculation made in the context of the rugged Mueller potential. The images along the string are shown as black dots. The straight black lines show the boundaries of the Voronoi cells associated with each image, and the white and gray dots are the last 1000 positions of the molecular-dynamics replicas used to perform the conditional sampling in these cells. In comparison with **Figure 8**, the replica remains confined in the transition tube, concentrating most of the flux of reactive trajectories shown in **Figure 8**, and therefore permits the analysis of the tube's characteristics (e.g., width).

5.2. Free Energy and Rate Calculations

As previously noted (22; see also 75) the free energy of the reaction defined in Equation 53 can be estimated in the context of the finite-temperature string method. This free energy can be related to the equilibrium probability of finding the system in each Voronoi cell B_i , which can itself be calculated by estimating the probability fluxes in and out of these cells by monitoring the rate at which the MD replica collides with the boundary of the cells (see 8 and 22 for details).

The setup with Voronoi cells used in the finite-temperature string method can also be conveniently combined with several techniques introduced recently to calculate reaction rates, e.g., milestoning (44, 76–80), transition interface sampling (81–83), and forward flux sampling (84–86). All these methods analyze a reaction by decomposing it into a series of steps, each of which corresponds to the system moving from one intermediate to another. These intermediates are called milestones in milestoning and interfaces in transition interface sampling and forward flux sampling, and a basic issue is where to place them as this choice affects the accuracy and/or efficiency of the procedures.

Recently (79) it has been proposed to use the boundaries of the Voronoi cells as intermediates along the string. In the context of Markovian milestoning, this leads to a reformulation in which all the relevant quantities in the method can be estimated by monitoring the evolution of the MD replica in the cells. Simulations confined to Voronoi cells can also be used to perform rate calculations à la transition interface sampling and forward flux sampling, again using the cell boundaries as interfaces (see 87). In this case, the procedure becomes a generalization of the nonequilibrium sampling method introduced in References 88 and 89 (for more details, see 8).

6. CONCLUSIONS

TPT calculates the relevant quantities associated with reactive events in terms of the committor functions, which in principle can be computed by solving Kolmogorov-type equations. However, these equations are formulated in a very high dimensional space. It is not practical to solve them either analytically or numerically, except for special cases (including the discrete state-space case discussed in Section 2.7, which is of interest). Therefore approximations have to be made to develop practical algorithms. Variants of the string method are obtained under the assumption that the flux of reactive trajectories is concentrated in a few localized thin tubes. However, TPT goes beyond the approximations made in the string method—it opens the door to other approaches that rely on different approximations.

It is interesting to make an analogy with quantum mechanics. Like the quantum many-body problem, the equation for the committor function is a partial differential equation in a very high dimensional space—an addition of one particle increases the dimensionality by three. Therefore, in practice, one has to make an approximation to reduce the complexity of the problem. Well-known approximate theories include the Hartree-Fock approximation and the Kohn-Sham density functional theory (90). These approximations reduce the problem from a $3N$ dimensional problem to N coupled three-dimensional problems. The story reviewed here bears some similar spirit: The Kolmogorov equations play the role of the quantum many-body problem. The reduced equation for the finite-temperature string method is an approximation. In fact, one can make similar approximations as in quantum mechanics, in principle. As an example, the Hartree type of approximation has been considered in Reference 91.

From a theoretical viewpoint, with TPT and related advances, it is now possible to discuss reactive events in complex systems in rather precise terms. Conceptually, we now begin to think of transition events in terms of the family of isocommittor surfaces or approximations thereof

that foliate the configuration space between the reactant and product states, in contrast to the classical viewpoint in terms of transition states or dividing surfaces. In practical terms, efficient numerical techniques such as the finite-temperature string method and TPS have been developed and applied to interesting and challenging problems in a variety of areas, for example, in chemistry, biology, and material science.

However, there are still many challenges that remain. One important issue is the sampling of the ensemble of transition tubes. In cases in which more than one transition tube contributes to the reactive events, or when the transition tubes themselves exhibit metastability, one has to exercise caution when using the string method or most other existing numerical algorithms because they are local in nature. It is possible to combine global search techniques with these local methods. Another challenge is to find effective collective variables in which localized transition tubes exist, even if they do not in the original variables. Finally, as hinted at above, it is of great interest to develop approaches that do not rely on the assumption of the localized tubes because the TPT formalism does not need it.

DISCLOSURE STATEMENT

The authors are not aware of any affiliations, memberships, funding, or financial holdings that might be perceived as affecting the objectivity of this review.

ACKNOWLEDGMENTS

The research described here has benefited greatly from our collaborators, including David Chandler, Giovanni Ciccotti, Matthias Heymann, Luca Maragliano, Christoph Schütte, Fabio Tal, Maddalena Venturoli, and, especially, Weiqing Ren. We also thank Maddalena Venturoli for **Figure 1** and Philipp Metzner for **Figures 3–6**. The work reviewed in this article was supported by NSF, ONR, and DOE through a variety of grants.

LITERATURE CITED

1. Eyring H. 1935. The activated complex and the absolute rate of chemical reactions. *Chem. Rev.* 17:65–77
2. Horiuti J. 1938. On the statistical mechanical treatment of the absolute rate of chemical reaction. *Bull. Chem. Soc. Jpn.* 13:210–16
3. Wigner E. 1938. The transition state method. *Trans. Faraday Soc.* 34:29–41
4. Bennett CH. 1975. Exact defect calculations in model substances. In *Diffusion in Solids: Recent Developments*, ed. AS Nowick, JJ Burton, pp. 73–113. New York: Academic
5. Chandler D. 1978. Statistical mechanics of isomerization dynamics in liquids and the transition state approximation. *J. Chem. Phys.* 68:2959–70
6. Keck J. 1962. Statistical investigation of dissociation cross-sections for diatoms. *Discuss. Faraday Soc.* 33:173–82
7. Yamamoto T. 1960. Quantum statistical mechanical theory of the rate of exchange chemical reactions in the gas phase. *J. Chem. Phys.* 33:281–89
8. E W, Vanden-Eijnden E. 2009. Transition path theory and path-finding algorithms for the study of rare events. Extended version available from the ArXiv
9. Pratt L. 1986. A statistical method for identifying transition states in high dimensional problems. *J. Chem. Phys.* 85:5045–48
10. Bolhuis P. 2003. Transition-path sampling of β -hairpin folding. *Proc. Natl. Acad. Sci. USA* 100:12129–34
11. Bolhuis P, Chandler D, Dellago C, Geissler P. 2002. Transition path sampling: throwing ropes over rough mountain passes, in the dark. *Annu. Rev. Phys. Chem.* 53:291–318
12. E W, Vanden-Eijnden E. 2006. Towards a theory of transition paths. *J. Stat. Phys.* 123:503–23

13. Metzner P, Schütte C, Vanden-Eijnden E. 2006. Illustration of transition path theory on a collection of simple examples. *J. Chem. Phys.* 125:084110
14. Metzner P, Schütte C, Vanden-Eijnden E. 2009. Transition path theory for Markov jump processes. *Multiscale Model. Sim.* 7:1192–219
15. Vanden-Eijnden E. 2006. Transition path theory. In *Computer Simulations in Condensed Matter: From Materials to Chemical Biology*, Vol. 1, ed. M Ferrario, G Ciccotti, K Binder, pp. 439–78. Berlin: Springer
16. E W, Ren W, Vanden-Eijnden E. 2002. String method for the study of rare events. *Phys. Rev. B* 66:052301
17. E W, Ren W, Vanden-Eijnden E. 2005. Finite temperature string method for the study of rare events. *J. Phys. Chem. B* 109:6688–93
18. E W, Ren W, Vanden-Eijnden E. 2005. Transition pathways in complex systems: reaction coordinates, isocommittor surfaces, and transition tubes. *Chem. Phys. Lett.* 413:242–47
19. Maragliano L, Fischer A, Vanden-Eijnden E, Ciccotti G. 2006. String method in collective variables: minimum free energy paths and isocommittor surfaces. *J. Chem. Phys.* 125:024106
20. Maragliano L, Vanden-Eijnden E. 2007. On-the-fly string method for minimum free energy paths calculation. *Chem. Phys. Lett.* 446:182–90
21. Ren W, Vanden-Eijnden E, Maragakis P, E W. 2005. Transition pathways in complex systems: application of the finite-temperature string method to the alanine dipeptide. *J. Chem. Phys.* 123:134109
22. Vanden-Eijnden E, Venturoli M. 2009. Revisiting the finite temperature string method for the calculation of reaction tubes and free energies. *J. Chem. Phys.* 130:194103
23. Bussi G, Donadio D, Parrinello M. 2007. Canonical sampling through velocity rescaling. *J. Chem. Phys.* 126:014101
24. Leimkuhler B, Legoll F, Noorizadeh E. 2008. A temperature control technique for nonequilibrium molecular simulation. *J. Chem. Phys.* 128:074105
25. Bussi G, Zykova-Timan T, Parrinello M. 2009. Isothermal-isobaric molecular dynamics using stochastic velocity rescaling. *J. Chem. Phys.* 130:074101
26. Doob JL. 2001 (1984). *Classical Potential Theory and Its Probabilistic Counterpart*. Berlin: Springer-Verlag
27. Sznitman A-S. 1998. *Brownian Motion, Obstacles and Random Media*. Springer Monogr. Math. Berlin: Springer-Verlag
28. Bass RF. 1997. *Diffusions and Elliptic Operators: Probability and Its Applications*. New York: Springer Verlag
29. Hummer G. 2004. From transition paths to transition states and rate coefficients. *J. Chem. Phys.* 120:516–23
30. Berezhkovskii A, Hummer G, Szabo A. 2009. Reactive flux and folding pathways in network models of coarse-grained protein dynamics. *J. Chem. Phys.* 130:205102
31. Venturoli M, Vanden-Eijnden E, Ciccotti G. 2009. Kinetics of phase transitions in two dimensional Ising models studied with the string method. *J. Math. Chem.* 45:188–222
32. Buchete N, Hummer G. 2008. Coarse master equations for peptide folding dynamics. *J. Phys. Chem. B* 112:6057–69
33. Chodera JD, Singhal N, Pande VS, Dill KA, Swope WC. 2007. Automatic discovery of metastable states for the construction of Markov models of macromolecular conformational dynamics. *J. Chem. Phys.* 126:155101
34. Hummer G, Kevrekidis IG. 2003. Coarse molecular dynamics of a peptide fragment: free energy, kinetics, and long-time dynamics computation. *J. Chem. Phys.* 118:10762–73
35. Krivov S, Karplus M. 2004. Free energy disconnectivity graphs: application to peptide models. *J. Chem. Phys.* 117:10894–903
36. Noe F, Horenko I, Schütte C, Smith J. 2007. Hierarchical analysis of conformational dynamics in biomolecules: transition networks of metastable states. *J. Chem. Phys.* 126:155102
37. Pan AC, Roux B. 2008. Building Markov state models along pathways to determine free energies and rates of transitions. *J. Chem. Phys.* 129:064107
38. Shalloway D. 1996. Macrostates of classical stochastic systems. *J. Chem. Phys.* 105:9986–10007
39. Sriraman S, Kevrekidis IG, Hummer G. 2005. Coarse master equation from Bayesian analysis of replica molecular dynamics simulations. *J. Phys. Chem. B* 109:6479–84
40. Swope W, Pitera J, Suits F. 2004. Describing protein folding kinetics by molecular dynamics simulations. 1. Theory. *J. Phys. Chem. B* 108:6571–81

41. Swope W, Pitera J, Suits F, Pitman M, Eleftheriou M, et al. 2004. Describing protein folding kinetics by molecular dynamics simulations. 2. Example applications to alanine dipeptide and β -hairpin peptide. *J. Phys. Chem. B* 108:6582–94
42. Tal F, Vanden-Eijnden E. 2006. Transition state theory and dynamical corrections in ergodic systems. *Nonlinearity* 19:501–10
43. Vanden-Eijnden E, Tal F. 2005. Transition state theory: variational formulation, dynamical corrections, and error estimates. *J. Chem. Phys.* 123:184103
44. Vanden-Eijnden E, Venturoli M, Ciccotti G, Elber R. 2008. On the assumptions underlying milestoning. *J. Chem. Phys.* 129:174102
45. Branduardi D, Gervasio FL, Parrinello M. 2007. From a to b in free energy space. *J. Chem. Phys.* 126:054103
46. Berkowitz M, Morgan JD, McCammon JA, Northrup SH. 1983. Diffusion-controlled reactions: a variational formula for the optimum reaction coordinate. *J. Chem. Phys.* 79:5563–65
47. E W, Vanden-Eijnden E. 2004. Metastability, conformation dynamics, and transition pathways in complex systems. In *Multiscale Modelling and Simulation*, ed. S Attinger, P Koumoutsakos, pp. 35–68. New York: Springer
48. Hastie T. 1984. *Principal curves and surfaces*. PhD thesis. Stanford Univ.
49. Hastie T, Tibshirani R, Friedman JH. 2001. *The Elements of Statistical Learning: Data Mining, Inference, and Prediction*. New York: Springer
50. Nocedal J, Wright S. 1999. *Numerical Optimization*. New York: Springer
51. Henkelman G, Jónsson H. 1999. A dimer method for finding saddle points on high dimensional potential surfaces using only first derivatives. *J. Chem. Phys.* 111:7010–22
52. Fischer S, Karplus M. 1992. Conjugate peak refinement: an algorithm for finding reaction paths and accurate transition states in systems with many degrees of freedom. *Chem. Phys. Lett.* 194:252–61
53. Brower RC, Kessler DA, Koplik J, Levine H. 1983. Geometrical approach to moving-interface dynamics. *Phys. Rev. Lett.* 51:1111–14
54. Brower RC, Kessler DA, Koplik J, Levine H. 1984. Geometrical models of interface evolution. *Phys. Rev. A* 29:1335–42
55. E W, Ren W, Vanden-Eijnden E. 2007. Simplified and improved string method for computing the minimum energy paths in barrier-crossing events. *J. Chem. Phys.* 126:164103
56. Ren W. 2003. Higher order string method for finding minimum energy paths. *Comm. Math. Sci.* 1:377–84
57. Henkelman G, Jónsson H. 2000. Improved tangent estimate in the nudged elastic band method for finding minimum energy paths and saddle points. *J. Chem. Phys.* 113:9978–85
58. Burger S, Yang W. 2006. Quadratic string method for determining the minimum-energy path based on multiobjective optimization. *J. Chem. Phys.* 124:054109
59. Peters B, Heyden A, Bell AT, Chakraborty A. 2004. A growing string method for determining transition states: comparison to the nudged elastic band and string methods. *J. Chem. Phys.* 120:7877–86
60. Kanai Y, Tilocca A, Selloni A, Car R. 2004. First-principles string molecular dynamics: an efficient approach for finding chemical reaction pathways. *J. Chem. Phys.* 121:3359–67
61. Miller TF III, Vanden-Eijnden E, Chandler D. 2007. Solvent coarse-graining and the string method applied to the hydrophobic collapse of a hydrated chain. *Proc. Natl. Acad. Sci. USA* 104:14559–64
62. Khavrutskii IV, Arora K, Brooks CL 3rd. 2006. Harmonic Fourier beads method for studying rare events on rugged energy surfaces. *J. Chem. Phys.* 125:174108
63. Khavrutskii IV, McCammon JA. 2007. Generalized gradient-augmented harmonic Fourier beads method with multiple atomic and/or center-of-mass positional restraints. *J. Chem. Phys.* 127:124901
64. Pan AC, Sezer D, Roux B. 2008. Finding transition pathways using the string method with swarms of trajectories. *J. Phys. Chem. B* 112:3432–40
65. Olender R, Elber R. 1997. Yet another look at the steepest descent path. *J. Mol. Struct. Theochem.* 398:63–71
66. Vanden-Eijnden E, Heymann M. 2008. The geometric minimum action method for computing minimum energy paths. *J. Chem. Phys.* 128:061103
67. Dellago C, Bolhuis PG, Geissler PL. 2002. Transition path sampling. *Adv. Chem. Phys.* 123:1–78
68. Elber R, Karplus M. 1987. A method for determining reaction paths in large molecules: application to myoglobin. *Chem. Phys. Lett.* 139:375–80

69. Ulitsky A, Elber R. 1990. A new technique to calculate steepest descent paths in flexible polyatomic systems. *J. Chem. Phys.* 92:1510–11
70. Gillilan RE, Lilien RH. 2004. Optimization and dynamics of protein-protein complexes using b-splines. *J. Comput. Chem.* 25:1630–46
71. Henkelman G, Jóhannesson G, Jónsson H. 2000. Methods for finding saddle points and minimum energy paths. *Prog. Theor. Chem. Phys.* 111:269–300
72. Jónsson H, Mills G, Jacobsen KW. 1998. Nudged elastic band method for finding minimum energy paths of transitions. In *Classical and Quantum Dynamics in Condensed Phase Simulations*, ed. BJ Berne, G Ciccotti, DF Coker, pp. 385–404. Singapore: World Sci.
73. Sheppard D, Terrell R, Henkelman G. 2008. Optimization methods for finding minimum energy paths. *J. Chem. Phys.* 128:134106
74. Henkelman G, Uberuaga BP, Jónsson H. 2000. A climbing image nudged elastic band method for finding saddle points and minimum energy paths. *J. Chem. Phys.* 113:9901–4
75. Vanden-Eijnden E. 2009. Some recent techniques for free energy calculations. *J. Comput. Phys.* 30:1737–47
76. Elber R. 2007. A milestoning study of the kinetics of an allosteric transition: atomically detailed simulations of deoxy Scapharca hemoglobin. *Biophys. J.* 92:L85–87
77. Faradjian AK, Elber R. 2004. Computing time scales from reaction coordinates by milestoning. *J. Chem. Phys.* 120:10880–89
78. Shalloway D, Faradjian AK. 2006. Efficient computation of the first passage time distribution of the generalized master equation by steady-state relaxation. *J. Chem. Phys.* 124:054112
79. Vanden-Eijnden E, Venturoli M. 2009. Markovian milestoning with Voronoi tessellations. *J. Chem. Phys.* 130:194101
80. West AMA, Elber R, Shalloway D. 2007. Extending molecular dynamics timescales with milestoning: example of complex kinetics in a solvated peptide. *J. Chem. Phys.* 126:145104
81. Moroni D, Bolhuis PG, van Erp TS. 2004. Rate constants for diffusive processes by partial path sampling. *J. Chem. Phys.* 120:4055–65
82. Moroni D, van Erp TS, Bolhuis PG. 2004. Investigating rare events by transition interface sampling. *Phys. A* 340:395–401
83. van Erp TS, Moroni D, Bolhuis PG. 2003. A novel path sampling method for the calculation of rate constants. *J. Chem. Phys.* 118:7762–74
84. Allen RJ, Frenkel D, ten Wolde PR. 2006. Forward flux sampling-type schemes for simulating rare events: efficiency analysis. *J. Chem. Phys.* 124:194111
85. Allen RJ, Frenkel D, ten Wolde PR. 2006. Simulating rare events in equilibrium or nonequilibrium stochastic systems. *J. Chem. Phys.* 124:024102
86. Valeriani C, Allen RJ, Morelli MJ, Frenkel D, ten Wolde PR. 2007. Computing stationary distributions in equilibrium and nonequilibrium systems with forward flux sampling. *J. Chem. Phys.* 127:114109
87. Vanden-Eijnden E, Venturoli M. 2009. Exact rate calculations by trajectory parallelization and tilting. *J. Chem. Phys.* 131:044120
88. Dickson A, Warmflash A, Dinner AR. 2009. Nonequilibrium umbrella sampling in spaces of many order parameters. *J. Chem. Phys.* 130:074104
89. Warmflash A, Bhimalapuram P, Dinner AR. 2007. Umbrella sampling for nonequilibrium processes. *J. Chem. Phys.* 127:154112
90. Parr RG, Yang W. 1989. *Density Functional Theory of Atoms and Molecules*. New York: Oxford Univ. Press
91. Friescke G, Junge O, Koltai P. 2009. Mean field approximation in conformation dynamics. *Multiscale Model. Simul.* In press



Contents

On Walking in the Footprints of Giants <i>Marilyn E. Jacox</i>	1
Novel Computational Methods for Nanostructure Electronic Structure Calculations <i>Lin-Wang Wang</i>	19
Hyper-Raman Scattering by Molecular Vibrations <i>Anne Myers Kelley</i>	41
Chemistry of Hofmeister Anions and Osmolytes <i>Yanjie Zhang and Paul S. Cremer</i>	63
Tuned Range-Separated Hybrids in Density Functional Theory <i>Roi Baer, Ester Livshits, and Ulrike Salzner</i>	85
Subcellular Dynamics and Protein Conformation Fluctuations Measured by Fourier Imaging Correlation Spectroscopy <i>Eric N. Senning and Andrew H. Marcus</i>	111
Oxide Surface Science <i>Ulrike Diebold, Shao-Chun Li, and Michael Schmid</i>	129
The Diabatic Picture of Electron Transfer, Reaction Barriers, and Molecular Dynamics <i>Troy Van Voorhis, Tim Kowalczyk, Benjamin Kaduk, Lee-Ping Wang, Chiao-Lun Cheng, and Qin Wu</i>	149
Electrostatics of Strongly Charged Biological Polymers: Ion-Mediated Interactions and Self-Organization in Nucleic Acids and Proteins <i>Gerard C.L. Wong and Lois Pollack</i>	171
Dynamics on the Way to Forming Glass: Bubbles in Space-Time <i>David Chandler and Juan P. Garrahan</i>	191
Functional Motifs in Biochemical Reaction Networks <i>John J. Tyson and Béla Novák</i>	219

Electronic Properties of Nonideal Nanotube Materials: Helical Symmetry Breaking in DNA Hybrids <i>Slava V. Rotkin</i>	241
Molecular Structural Dynamics Probed by Ultrafast X-Ray Absorption Spectroscopy <i>Christian Bressler and Majed Chergui</i>	263
Statistical Mechanical Concepts in Immunology <i>Arup K. Chakraborty and Andrej Košmrlj</i>	283
Biological Cluster Mass Spectrometry <i>Nicholas Winograd and Barbara J. Garrison</i>	305
Bio-Enabled Synthesis of Metamaterials <i>Christopher C. DuFort and Bogdan Dragnea</i>	323
Superresolution Imaging using Single-Molecule Localization <i>George Patterson, Michael Davidson, Suliana Manley, and Jennifer Lippincott-Schwartz</i>	345
From Artificial Atoms to Nanocrystal Molecules: Preparation and Properties of More Complex Nanostructures <i>Charina L. Choi and A. Paul Alivisatos</i>	369
Transition-Path Theory and Path-Finding Algorithms for the Study of Rare Events <i>Weinan E and Eric Vanden-Eijnden</i>	391
Complex Fluids: Probing Mechanical Properties of Biological Systems with Optical Tweezers <i>H. Daniel Ou-Yang and Ming-Tzo Wei</i>	421
Enhanced Sampling of Nonequilibrium Steady States <i>Alex Dickson and Aaron R. Dinner</i>	441
Fluctuations in Biological and Bioinspired Electron-Transfer Reactions <i>Spiros S. Skourtis, David H. Waldeck, and David N. Beratan</i>	461

Indexes

Cumulative Index of Contributing Authors, Volumes 57–61	487
Cumulative Index of Chapter Titles, Volumes 57–61	490

Errata

An online log of corrections to *Annual Review of Physical Chemistry* articles may be found at <http://physchem.annualreviews.org/errata.shtml>